

THESIS FOR THE DEGREE OF DOCTOR OF PHILOSOPHY

High Speed Vertical Cavity Surface Emitting  
Lasers for Short Reach Communication

PETTER WESTBERGH

Photonics Laboratory  
Department of Microtechnology and Nanoscience (MC2)  
CHALMERS UNIVERSITY OF TECHNOLOGY  
Göteborg, Sweden, 2011

# High Speed Vertical Cavity Surface Emitting Lasers for Short Reach Communication

Petter Westbergh

Göteborg, April 2011

©PETTER WESTBERGH, 2011

ISBN 978-91-7385-527-3

Doktorsavhandling vid Chalmers Tekniska Högskola  
Ny serie 3208  
ISSN 0346-718X

Technical Report MC2-190  
ISSN 1652-0769

Photonics Laboratory  
Department of Microtechnology and Nanoscience (MC2)  
Chalmers University of Technology

SE-412 96 Göteborg, Sweden  
Phone: +46 (0) 31 772 1000

**Front cover illustration:** Scanning electron microscope image of fully fabricated high speed VCSELs on chip.

Printed by Bibliotekets reproservice, Chalmers University of Technology  
Göteborg, Sweden, April 2011

# High Speed Vertical Cavity Surface Emitting Lasers for Short Reach Communication

Petter Westbergh

Photonics Laboratory  
Department of Microtechnology and Nanoscience (MC2)  
Chalmers University of Technology

SE-412 96 Göteborg, Sweden

## Abstract

The vertical cavity surface emitting laser (VCSEL) is a low cost light source with attractive performance characteristics such as low power consumption, high speed capabilities at low currents, and a circular output beam. These features have made the VCSEL an established component in digital communication networks, particularly in short reach optical data transmission applications where links consisting of GaAs-based 850 nm VCSELs and multimode fiber have become the standard solution. However, VCSELs available on the market today are limited to bit-rates of  $\sim 10$  Gbit/s and as current trends point towards single channel bit-rates being standardized and implemented far beyond this point, the development of higher speed VCSELs is crucial to meet the market's need for higher speed digital communication services in the near future.

The objective of this work has been to extend the maximum possible data transmission rate for 850 nm VCSELs beyond the bit-rate limit of today's commercially available devices. The work includes detailed studies of intrinsic and extrinsic device characteristics of importance for high speed performance and illuminates design trade-offs necessary for optimized performance. By tailoring the epitaxial and component design we demonstrate that 10 Gbit/s is far from the end point for VCSEL technology. Using strained InGaAs quantum wells (QWs) for high differential gain, a thin graded separate confinement heterostructure (SCH) for short carrier capture time, a binary compound in the bottom mirror for improved thermal conductivity, and a component design optimized for low electrical parasitics we are able to reach a modulation bandwidth of 20 GHz and demonstrate error-free data transmission at bit-rates up to 32 Gbit/s in the first generation devices. After optimization of the photon lifetime and a further reduction of electrical parasitics, we ultimately reach a record high modulation bandwidth of 23 GHz and demonstrate 40 Gbit/s error-free data transmission for the second generation 850 nm VCSELs.

**Keywords:** Semiconductor laser, vertical cavity surface emitting laser (VCSEL), GaAs, InGaAs, laser dynamics, high speed modulation, fabrication



# List of papers

This thesis is based on the following appended papers:

- [A] **P. Westbergh**, J. S. Gustavsson, Å. Haglund, H. Sunnerud, and A. Larsson, "Large aperture 850 nm VCSELs operating at bit rates up to 25 Gbit/s," *Electron. Lett.*, vol. 44, no. 15, pp. 907-908, July 2008.
- [B] **P. Westbergh**, J. S. Gustavsson, Å. Haglund, M. Sköld, A. Joel, and A. Larsson, "High-speed, low-current-density 850 nm VCSELs," *IEEE J. Sel. Topics Quantum Electron.*, vol. 15, no. 3, pp. 694-703, May/June 2009 (invited paper).
- [C] **P. Westbergh**, J. S. Gustavsson, Å. Haglund, A. Larsson, F. Hopfer, G. Fiol, D. Bimberg and A. Joel, "32 Gbit/s multimode fibre transmission using high-speed, low current density 850 nm VCSEL," *Electron. Lett.*, vol. 45, no. 7, pp. 366-368, March 2009.
- [D] Y. Ou, J. S. Gustavsson, **P. Westbergh**, Å. Haglund, A. Larsson and A. Joel, "Impedance characteristics and parasitic speed limitations of high-speed 850-nm VCSELs," *IEEE Photon. Technol. Lett.*, vol. 21, no. 24, pp. 1840-1842, December 2009.
- [E] S. B. Healy, E. P. O'Reilly, J. S. Gustavsson, **P. Westbergh**, Å. Haglund, A. Larsson and A. Joel, "Active region design for high-speed 850-nm VCSELs," *IEEE J. Quantum Electron.*, vol. 46, no. 4, pp. 506-512, April 2010.
- [F] **P. Westbergh**, J. S. Gustavsson, B. Kögel, Å. Haglund, A. Larsson and A. Joel, "Speed enhancement of VCSELs by photon lifetime reduction," *Electron. Lett.*, vol. 46, no. 13, pp. 938-940, June 2010.
- [G] **P. Westbergh**, J. S. Gustavsson, B. Kögel, Å. Haglund, A. Larsson, A. Mutig, A. Nadtochiy, D. Bimberg and A. Joel, "40 Gbit/s error-free operation of oxide-confined 850 nm VCSEL," *Electron. Lett.*, vol. 46, no. 14, pp. 1014-1016, July 2010.
- [H] **P. Westbergh**, J. S. Gustavsson, B. Kögel, Å. Haglund and A. Larsson, "Impact of photon lifetime on high speed VCSEL performance," *IEEE J. Sel. Topics Quantum Electron.*, accepted for publication 2011 (invited paper).



# Acknowledgement

Many people have contributed to the work of this thesis and I am grateful to all of you. First of all, I want to express my gratitude to my supervisor and examiner Prof. Anders Larsson for giving me the opportunity to work in this exciting project and for excellent support throughout these four years of research. I have also had the benefit of having two excellent assistant supervisors; Johan Gustavsson, who has helped me with measurements and in deciphering and understanding the results, and Åsa Haglund, who first introduced me to the world of VCSEL processing and showed me the ropes around the cleanroom. Johan and Åsa were also my Master Thesis advisors and are thus responsible for first introducing me to VCSELs and for sparking my interest to pursue PhD studies in the same field – thank you for that! Device fabrication has been a significant part of this project and I have consequently spent quite some time using the cleanroom facilities here at MC2. After having visited process labs at a number of different universities I have come to realize just how excellent our facilities here really are. So thank you to the staff in the MC2 Process Laboratory for keeping such a nice lab and for all of the much appreciated assistance!

Of course, I also want to acknowledge my past and present colleagues here at the Photonics Laboratory for making this such an exciting and inspiring place to work. Thank you Ben for all the help and for being a true VCSEL guy. Many thanks to all my fellow PhD students for all the distractions, both during work and after working hours. Special thanks to Göran, Calle Be, Ben, Yuxin, Huan, and Rambo for making conference trips and summerschools such nice memories.

Finally, I am grateful to my friends and family for reminding me of the world outside of the lab. Erik and my liften friends deserves special mention for all the great events over the past years. Thank you Erika for all the fun times and for helping me survive these years – I am not sure what I would have done without you. Also, thank you Johan and Katarina for all the Friday nights and for everything else, you are great!

This work was financially supported by the Swedish Foundation for Strategic Research (SSF) and the European project VISIT (FP7-224211). I would also like to acknowledge IQE Europe for supplying the epitaxial VCSEL material.

Petter Westbergh

*Göteborg  
April 2011*



# Table of contents

|   |            |
|---|------------|
| <b>Abstract</b>   | <b>i</b>   |
| <b>List of papers</b>                                       | <b>iii</b> |
| <b>Acknowledgement</b>                                      | <b>v</b>   |
| <b>1 Introduction</b>                                       | <b>1</b>   |
| 1.1 Trends in short reach communication . . . . .           | 2          |
| 1.2 State-of-the-art . . . . .                              | 3          |
| 1.2.1 850 nm VCSELs . . . . .                               | 4          |
| 1.2.2 980–1100 nm VCSELs . . . . .                          | 5          |
| 1.3 Organization of thesis . . . . .                        | 6          |
| <b>2 Basic VCSEL properties</b>                             | <b>7</b>   |
| 2.1 Basic semiconductor laser principles . . . . .          | 7          |
| 2.2 VCSEL structure and properties . . . . .                | 10         |
| 2.2.1 Optical, thermal, and electrical properties . . . . . | 10         |
| 2.2.2 Transverse confinement . . . . .                      | 13         |
| <b>3 Dynamic VCSEL properties</b>                           | <b>17</b>  |
| 3.1 Rate equations . . . . .                                | 17         |
| 3.2 Small signal modulation . . . . .                       | 18         |
| 3.3 High speed VCSEL design . . . . .                       | 21         |
| 3.3.1 Active region . . . . .                               | 22         |
| 3.3.2 Damping . . . . .                                     | 24         |
| 3.3.3 Thermal effects . . . . .                             | 26         |
| 3.3.4 Electrical parasitics . . . . .                       | 29         |
| <b>4 VCSEL fabrication</b>                                  | <b>33</b>  |
| 4.1 Epitaxial material . . . . .                            | 33         |
| 4.2 General processing techniques . . . . .                 | 34         |
| 4.2.1 Lithography . . . . .                                 | 34         |
| 4.2.2 Thin film deposition . . . . .                        | 35         |
| 4.2.3 Etching . . . . .                                     | 36         |
| 4.2.4 Wet oxidation . . . . .                               | 36         |
| 4.3 Fabrication process for high speed VCSELs . . . . .     | 37         |

|  |           |
|--|-----------|
| <b>5 High speed measurements</b>               | <b>41</b> |
| 5.1 Small signal modulation response . . . . . | 41        |
| 5.2 Electrical impedance . . . . .             | 42        |
| 5.3 Transmission experiments . . . . .         | 43        |
| <b>6 Summary of papers</b>                     | <b>47</b> |
| <b>References</b>                              | <b>51</b> |
| <b>Papers A–C</b>                              | <b>61</b> |

# 1 Introduction

At the time of writing this text, a google search for "we live in the information age" rendered roughly 1 700 000 hits. Taking this high number as an indication that we in fact do live in the information age, we may ask ourselves: how did we end up here? Many would argue that along with the development of the personal computer, Internet paved the way: information is now widely available to everyone with access to a computer and an Internet connection<sup>1</sup>. Hidden from plain sight, the backbone of the Internet consists of fiber-optic cables wherein laser signals are used to transmit vast amounts of data across the planet at aggregate bit-rates of many Tbit/s.

There are a number of reasons why light can be used as an efficient carrier of information. First, the high carrier frequency (greater than 100 THz in the so-called communication bands) makes it possible to modulate the signal with enormous amounts of information without significantly affecting the properties of the light. Second, the propagation of the light is highly insensitive to electromagnetic interference. Third, the short wavelength ( $\sim 1\ \mu\text{m}$ ) makes it possible to propagate the light in optical fibers. These are thin, inexpensive, dielectric waveguides with extremely small attenuation of the signal compared to electrical high speed interconnects<sup>2</sup>. With the development of the semiconductor laser [1], the low loss optical fiber [2, 3], and the fiber amplifier [4], fiber-optics have therefore revolutionized the way we communicate.

Although invented already in 1979 [5], the vertical cavity surface emitting laser (VCSEL) would not seriously leave the laboratory until the second half of the 1990s with the inclusion of a short wavelength multimode fiber standard for short distances in the Gigabit Ethernet (GbE) and Fibre Channel (FC) technologies. Interest was fueled by the rapid expansion of the Internet and the GaAs-based VCSEL emerged as a low cost, high speed, and highly reliable source alternative for optical interconnects [6]. During the past decade, directly modulated VCSELs have proliferated in local area network (LAN) environments, including optical networks in data centers (storage area networks, SANs) and high performance computing (HPC) systems, gradually replacing galvanic interconnects and other laser sources owing to increasingly stringent requirements on high speed, high efficiency, and low cost [7]. These data communication (dat-

---

<sup>1</sup>As of 2010, approximately 29% of the world's population have Internet access, see <http://www.internetworldstats.com/stats.htm>.

<sup>2</sup>At the minimum attenuation wavelength of  $1.55\ \mu\text{m}$ , the power loss after propagating a signal over one kilometer low loss silica fiber is only  $\sim 4\%$ !

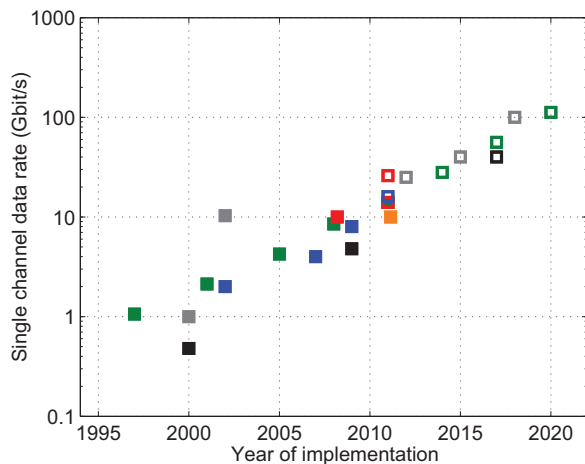


Figure 1.1: Single lane data rates for various LAN, SAN, HPC, and consumer standards vs. year of implementation. Open symbols indicate predictions [7, 9, 10].

acom) networks<sup>3</sup> consist of relatively short links (< 300 m) and are based on multimode fiber (OM2, OM3, and OM4), optimized for a wavelength of 850 nm. Highly multimode VCSELs and multimode fibers are used to relax packaging and fabrication tolerances and to make the links less susceptible to effects from mode-selective loss and optical feedback [8].

## 1.1 Trends in short reach communication

Fig. 1.1 shows the single lane data rates for various LAN, SAN, and HPC standard protocols plotted versus year of implementation. For electrical interconnects, attenuation increases with frequency and at the 10+ Gbit/s speeds where current standards are being set, galvanic interconnects are starting to run into serious trouble due to excessive losses. These necessitate increased power budgets which is problematic since already in 2005, data centers represented a staggering 1% of the world's total electricity consumption [11]. Consequently, speed as well as power efficiency is key and optical solutions are required at ever-shorter distances. Also included in Fig. 1.1 are the USB (USB 3.0 is at 4.8 Gbit/s) and Thunderbolt (10 Gbit/s) consumer standards. Currently, these support only electrical interconnects but Intel's Thunderbolt technology, which was originally conceived as an optical technology codenamed Light Peak, will include VCSEL-based fiber-optics in future versions<sup>4</sup> and it is likely that the same will be the case for USB 4.0<sup>5</sup> [7]. The emerging arena of consumer electronics will result in an enormous volume increase for high speed VCSEL production.

<sup>3</sup>Long range links are usually referred to as telecommunication (telecom) networks.

<sup>4</sup>See <http://www.intel.com/technology/io/thunderbolt/>.

<sup>5</sup>Initially, optical connections were rumored to be included also in the USB 3.0 standard.

Active optical cables (AOCs) represent an already rapidly growing market segment for optical interconnects and is expected to reach \$1.4 billion in revenues by 2015<sup>6</sup>. In addition to advantages compared to copper-based interconnects such as longer possible transmission distances and less weight and volume, the popularity is in large due to the simplicity for the end user; AOCs provide a pluggable electrical connector at both ends and the optical links are completely hidden within the cable. The only part standardized is the connector itself and what is contained within the cable is up to the manufacturer. This resolves issues like eye-safety and connector cleanliness otherwise associated with optical interconnects. Requirements on wavelength are also relaxed and *e.g.* 980 or 1100 nm may be used in place of 850 nm VCSELs. HPCs have used optical modules (including AOCs) for rack-to-rack interconnects, *i.e.* for connecting entire racks of servers, already for many years. IBM's supercomputer Blue Waters<sup>7</sup>, scheduled for 2011, will increase the level of integration and use more than one million VCSEL-based optical interconnects in intrarack configurations. With future generation exa-scale supercomputers, an even further level of integration between optics and CMOS is required and the number of optical links in a single HPC is predicted to rise into the 100s of millions from utilizing module-to-module interconnects via optical printed circuit boards [12]. Supercomputers are thus driving the development of large-scale deployment and integration of optical transceivers and for module-to-module interconnects, high speed and efficiency VCSELs are attractive options as light sources.

However, the highest speed commercially available VCSELs today are designed for 10GbE and consequently limited to data rates of 10 Gbit/s. Even though VCSEL solutions for 16GFC (14 Gbit/s) will be available from major vendors during 2011 [13,14], significant improvements are necessary to meet near future demands. It is within this context the work for this thesis has been conducted, with the goal of extending the maximum possible bandwidth of 850 nm VCSELs to allow for error-free data transmission at 40 Gbit/s and beyond.

## 1.2 State-of-the-art

Motivated by the trends described above, multiple research groups have spent considerable effort towards developing high speed VCSELs emitting around 850 and 980–1100 nm in the recent years. The effort has paid off and, as illustrated in Fig. 1.2, significant progress in the field of short wavelength VCSELs have been made in only a few years. In the following, a brief overview of the recent progress of state-of-the-art GaAs-based high speed VCSELs is presented, distinguishing between the different wavelength regions. Details on design considerations necessary to reach these levels of performance are more thoroughly discussed in Chapter 3.

---

<sup>6</sup>See <http://www.igigroup.com/st/pages/aoc.html>.

<sup>7</sup>See <http://www.ncsa.illinois.edu/BlueWaters/>.

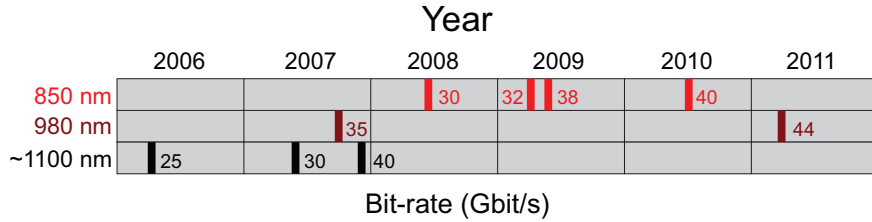


Figure 1.2: Timeline for first demonstrations at data rates of 25 Gbit/s and above for 850, 980, and  $\sim$ 1100 nm VCSELs. The 850 nm data rates at 30, 32, 38, and, 40 Gbit/s were reported in [15], Paper C, [16], and Paper G. At 980 nm, the 35 and 44 Gbit/s data rates are from [17] and [18], respectively. For wavelengths around 1100 nm, the bit-rates 25, 30, and 40 Gbit/s were reported in [19–21]

### 1.2.1 850 nm VCSELs

The standard wavelength used in current datacom protocols (*e.g.* Ethernet, Fibre Channel, Infiniband, etc.) is 850 nm and this is thus a wavelength of great importance. This is also where high speed multimode fiber is available and polymer waveguide loss is lower at 850 nm compared to the other wavelengths [22], giving a possible advantage for integration to optical printed circuit boards when relatively long ( $\sim$ 1 m) transmission distances are required [12]. Additionally, free carrier absorption loss is lowest at 850 nm due to thinner structures and lower free carrier absorption coefficient at shorter wavelengths. This allows for higher doping levels to be used and therefore potentially lower device resistance. However, there are a few drawbacks. Since GaAs is non-transparent at 850 nm, substrate emission, which is possible at 980–1100 nm, is not an option. This complicates compact integration with CMOS and also makes ternary distributed Bragg reflectors (DBRs) mandatory, thereby reducing thermal conductivity and impairing heat management. Still, 850 nm VCSELs remain dominant in datacom applications and this is the wavelength where the major vendors have their main activities.

Already in 2001, 20 Gbit/s operation with open eye-diagrams was demonstrated for an oxide confined 8  $\mu$ m aperture 850 nm VCSEL by IBM [23]. It would then take until 2008 to increase the bit-rate to 30 Gbit/s, a data rate first reached by Finisar using an oxide-implanted 6  $\mu$ m aperture VCSEL with a maximum bandwidth of 19 GHz [15]. This achievement marked the start of an intense period of research where the maximum bit-rate was brought from 20 to 40 Gbit/s in only two years. Later in 2008, we demonstrated open eyes at 25 Gbit/s (Paper A) and, in early 2009, broke the 30 Gbit/s barrier with error-free transmission over 50 m of OM3 fiber at 32 Gbit/s using a 9  $\mu$ m double layer aperture VCSEL with 20 GHz maximum bandwidth (Paper C). With a component and epitaxial design similar to ours, S. A. Blohkin *et al.* at Technische Universität Berlin (TUB) then raised the bar further by demonstrating error-free transmission at 38 Gbit/s with a 6  $\mu$ m aperture VCSEL only a few months later that same year [16]. The

40 Gbit/s barrier seemed elusive, but then in 2010 we managed to brake the 13 year old 850 nm modulation bandwidth record of K. Lear *et al.* at 21.5 GHz [24], reaching a 23 GHz maximum bandwidth using a 7  $\mu\text{m}$  aperture component (Paper F) and error-free transmission at 40 Gbit/s was finally demonstrated (Paper G). To the best of our knowledge, this is currently the world's fastest VCSEL operating at 850 nm.

### 1.2.2 980–1100 nm VCSELS

Due to the lack of suitable fiber, longer wavelength multimode VCSELS may not be practical for use up to the same distances as 850 nm devices, but the possibility of substrate emission make them attractive for potential chip-to-chip integration (distances  $\ll$  1 m) since a more compact package can be used [25]. Additionally, binary DBRs can be used to improve thermal conductivity which, in combination with advantages of deeper barriers to prevent carrier escape from the quantum wells (QWs), improve temperature stability. It is also possible to incorporate heavily strained InGaAs QWs which is beneficial for high speed performance. Combined with the research efforts, these characteristics have led to very impressive results in this wavelength region, bringing the highest demonstrated data-rate from 20 to 40 Gbit/s in a timespan less than two years.

In 2005, IBM demonstrated 20 Gbit/s open eye-diagrams at 980 nm within their "Terabus" program for optical interconnects [26,27]. This was followed by N. Suzuki *et al.* from NEC in Japan, who brought the bit-rate up to 25 Gbit/s in early 2006 with their oxide-implanted 1070 nm VCSELS [19]. NEC followed up their result in 2007 and demonstrated 30 Gbit/s error-free transmission, again using an oxide-implanted 1070 nm VCSEL [20]. Only a few months later, Y.C. Chang *et al.* from University of California at Santa Barbara countered with their multiple-oxide layer 3  $\mu\text{m}$  aperture 980 nm VCSEL, demonstrating error-free transmission at 35 Gbit/s [17]. The record would, however, not stand for long and in December 2007, NEC demonstrated 40 Gbit/s error-free transmission using a 1090 nm ion-implanted 6  $\mu\text{m}$  aperture tunnel-junction VCSEL [21]. It would then take until 2011 for a higher bit-rate to be reported by W. Hofmann *et al.* from TUB. Building on previous, impressive results with 20 Gbit/s transmission at up to 120°C [28] and 25 Gbit/s at up to 85°C [29], the group at TUB were able to demonstrate 44 Gbit/s error-free transmission at 980 nm [18].

Although not yet reaching the same speeds, the work by Furukawa Electric should also be mentioned in this context. For the intended application of chip-to-chip interconnects, they have demonstrated error-free transmission using high efficiency oxide confined 1060 nm VCSELS at 10 and 20 Gbit/s with only 140 and 160 fJ/bit of dissipated energy, respectively [30,31]. At the very short transmission distances that are considered for this application, the dissipated energy is a critical figure of merit and needs to be minimized in order to be competitive with existing electrical interconnects. The results from Furukawa represent considerable progress in this direction [32].

## 1.3 Organization of thesis

The target of this work has been focused on extending the possible data transmission rate towards 40 Gbit/s and beyond in multimode VCSELs operating at 850 nm. The thesis is organized as follows: Chapter 2 introduces the basic, static properties of semiconductor lasers in general with a particular focus on VCSELs. Chapter 3 is the main chapter and discusses high speed modulation properties of VCSELs and design considerations and trade-offs necessary for reaching high data rates. Processing techniques for the fabrication of the VCSELs are described in Chapter 4 and methods used for characterizing the dynamic properties of VCSELs are presented in Chapter 5. The thesis builds on the appended Papers A-H which are summarized in Chapter 6.

## 2 Basic VCSEL properties

Laser is an acronym for "Light Amplification by Stimulated Emission of Radiation". Even though the original meaning denotes a principle of operation rather than a device, the term laser is now mostly used for devices that produce light based on the laser principle. Much has happened in the more than 50 years since Theodore Maiman demonstrated the first laser in the form of an optically pumped ruby crystal in 1960 [33]. Today, the largest<sup>1</sup> and most powerful<sup>2</sup> laser is located at the National Ignition Facility in the United States where its 1.8 MJ ultraviolet laser pulses are used in fusion research [34]. At the other end of the scale, so-called plasmon lasers [35] have recently been realized with dimensions smaller than 100 nm [36]. The basic operating principle, however, remains the same independent of size and it is the stimulated emission process that gives laser light its unique properties of being highly coherent and monochromatic. These properties have resulted in a wide range of applications *e.g.* in manufacturing, medicine, metrology, data storage, spectroscopy, as a tool in scientific research, and, which is the focus of this thesis; communication. Even though there exists a large variety of different laser technologies, all lasers are essentially built up in the same way with a gain medium confined inside an optical resonator (cavity), often made up by two semitransparent mirrors. Light is amplified when energy is supplied to the gain medium (when the laser is pumped) and lasing occurs when the light field trapped in the cavity is able to repeat itself after one round trip. To get an output laser beam, at least one of the mirrors forming the resonator needs to have a reflectivity less than 100%.

### 2.1 Basic semiconductor laser principles

The gain medium in an electrically pumped semiconductor laser usually consists of a thin undoped (intrinsic) direct bandgap semiconductor sandwiched between *p*- and *n*-doped cladding layers with higher bandgap. When this *pin*-junction is forward biased, electrical carriers (electrons and holes) start to accumulate in the active (intrinsic) region and radiative transitions can occur. At a certain current, referred to as the threshold current, the optical gain equals the cavity losses (mirror losses and internal losses) and the lasing threshold is reached. The material gain required to reach threshold ( $g_{th}$ ) can be expressed as:

---

<sup>1</sup>The NIF laser is housed in a 10 story building the size of three football fields.

<sup>2</sup>The equivalent peak power is an impressive  $500 \cdot 10^{12}$  W.

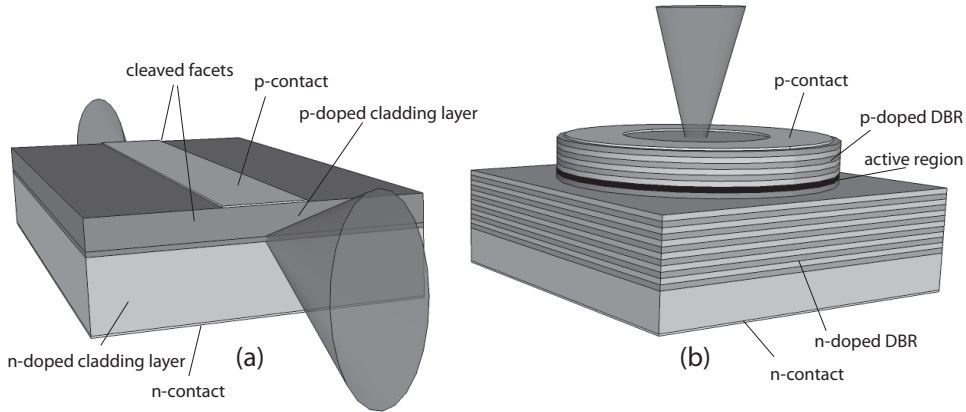


Figure 2.1: Different types of semiconductor lasers, (a) Fabry-Perot laser, (b) VCSEL.

$$g_{th} = \frac{1}{\Gamma} \left[ \alpha_i + \frac{1}{2L} \ln \left( \frac{1}{R_1 R_2} \right) \right] = \frac{1}{\Gamma} [\alpha_i + \alpha_m], \quad (2.1)$$

where  $\Gamma$  is the confinement factor<sup>3</sup>,  $\alpha_i$  the internal absorption,  $\alpha_m$  the mirror loss,  $L$  the cavity length, and  $R_1$  and  $R_2$  denote the respective mirror power reflectivities. Eq. 2.1 is referred to as the amplitude condition since it states that the amplitude of the electrical field must be the same after one round-trip in the cavity. At current injection levels exceeding the threshold current, all carriers injected in excess of the threshold carrier concentration are consumed by stimulated emission and contribute to the laser output. This leads to a self-regulating mechanism in the laser that clamps the carrier concentration and the gain at their threshold values and output power increases rapidly at currents beyond threshold.

For lasing to occur, the phase of the electric field must also repeat itself after one round-trip in the cavity, yielding the resonance condition:

$$\exp \left( -j \frac{2\pi}{\lambda_0/n_{eff}} \cdot 2L \right) = 1 \quad \Rightarrow \quad \lambda_0 = \frac{2L \cdot n_{eff}}{m}, \quad (2.2)$$

where  $\lambda_0$  is the vacuum wavelength,  $n_{eff}$  the effective refractive index of the lasing mode, and  $m$  an integer number. Eq. 2.2 states that only a certain, discrete number of resonant wavelengths are permitted. These constitute the so-called longitudinal modes of the laser. In practice, the amplitude condition can only be fulfilled for a narrow wavelength range where the optical gain is positive and therefore Eq. 2.1 sets a limit to the number of longitudinal modes that actually lase.

The simplest type of electrically pumped semiconductor laser is the Fabry-Perot (FP) laser, illustrated in Fig. 2.1 (a). This is a so-called edge emitting laser

<sup>3</sup>The confinement factor is defined as the overlap between the active region and the optical field:  $\Gamma = V_a/V_p$ , where  $V_a$  is the active region volume and  $V_p$  the volume of the lasing mode.

(EEL) where the cavity is formed in the plane of the active layer either by cleaving or etching the semiconductor crystal with the resulting semiconductor/air interfaces functioning as mirrors. In the GaAs system, this results in a typical power reflectivity of around 30% unless reflective or anti-reflective (AR) coatings are applied to the end facets. Because the smaller bandgap material in the active region has higher refractive index than the cladding layers, the active layer acts as a planar waveguide for the propagating optical field. Electrical carriers are injected via a stripe shaped contact on top of the laser. In this basic, gain-guided version of the FP laser, there is no inherent confinement of the optical field or of the carriers in the lateral direction, and loss of carriers injected to the active region through diffusion as well as optical losses tend to be high. More sophisticated versions utilize *e.g.* an etched ridge for lateral index guiding, or a regrown mesa for both photon guiding and lateral carrier confinement to improve efficiency.

Since the spatial dimensions of the waveguide of an FP laser is much larger in the direction parallel to the active layer than in the perpendicular, the resulting output beam has an elliptical cross-section (*c.f.* Fig. 2.1 (a)). This beam shape is problematic since it is poorly matched to the circular cross-section of an optical fiber, and corrective optics are necessary for high coupling efficiency. Another issue is the relatively long cavity of an FP laser (typically around 500  $\mu\text{m}$ ) which results in a narrow spacing of the longitudinal modes and, since the mirrors have virtually wavelength independent reflectivity and the gain spectrum is broad, leads to emission in multiple longitudinal modes. For many applications, single mode (single wavelength) emission is required and other EELs have therefore been developed.

Instead of using the end facets as mirrors, periodic gratings can be incorporated in the cavity to provide wavelength selective feedback and thus promote single longitudinal mode operation. When the grating is placed along the entire cavity, the laser is referred to as a distributed feedback (DFB) laser. Here, gain and feedback is provided throughout the length of the cavity. Another version is the DBR laser in which passive gratings are incorporated close to the end facets of the laser and gain is provided in a central region without gratings. In both these laser-types, high reflectivity can be engineered for a very narrow wavelength band, ensuring single mode emission as well as lower threshold currents compared to the basic FP laser. The drawback of these lasers is increased fabrication complexity and therefore increased cost. Cost is a general problem for EELs since each component essentially needs to be cleaved and packaged before testing and screening can take place.

Contrary to the EEL, the VCSEL, shown schematically in Fig. 2.1 (b), has a resonant cavity formed perpendicular to the plane of the active region layers. Feedback is provided by highly reflective DBR mirrors above and below this region, resulting in a very short effective resonator length (typically  $\sim 1 \mu\text{m}$ ) and a large longitudinal mode spacing making the VCSEL lase in a single longitudinal mode. However, large transverse dimensions (typically 10 – 20  $\mu\text{m}$ ) make the

cavity support multiple transverse modes and the VCSEL is thus inherently a multimode laser. The small volume of the active region and the laser cavity give advantages in terms of low threshold and operating currents and high modulation bandwidth at low currents. Surface emission allows for a circular output beam cross-section and efficient coupling to optical fiber. Even though the epitaxial growth of VCSELs is complicated with low tolerances for error, the small footprint<sup>4</sup> allows for  $10^4 - 10^5$  components to be fabricated on a single 3" wafer in one single process run. Combined with the possibility of on-wafer testing before dicing and packaging, this can reduce high volume fabrication costs dramatically compared to EELs<sup>5</sup>. Surface emission also allows for simple integration of components into 1D or 2D arrays, making *e.g.* compact multi-channel data transmission [37] or power scaling from a typical  $\sim 10$  mW in a single VCSEL to well above 100 W [38] possible for 2D arrays.

In the following, VCSEL design and properties are discussed in more detail.

## 2.2 VCSEL structure and properties

### 2.2.1 Optical, thermal, and electrical properties

Since the radiation from stimulated emission in a VCSEL propagates in the direction perpendicular to the plane of the active region layers, it is only amplified during a limited part of the cavity round trip. To provide sufficient gain for lasing, the active region typically consists of multiple QWs sandwiched between higher bandgap barriers in a separate confinement heterostructure (SCH) and placed in an antinode of the optical field. For a  $1\lambda$  thick SCH, the number of QWs is limited by the finite width of the central antinode of the optical field and the optimal number balances the increase in gain length and the reduction in confinement factor with increased number of QWs [39]. The properties of the active region material sets an upper limit for what performance can be reached in the VCSEL. The most mature VCSEL technology is based on the GaAs material system with AlGaAs DBRs. Using various QW materials, emission wavelengths in the range 630-1300 nm can be reached in devices based on GaAs wafers. The first commercially available VCSEL (by Honeywell<sup>6</sup> in 1996) utilized GaAs QWs to produce 850 nm emission and this wavelength continues to be of great importance since it is the standard for short reach optical communication links. Longer wavelengths (1.3-2.3  $\mu\text{m}$ ) can be reached using the InP material system and GaSb based VCSELs have recently been demonstrated reaching wavelengths up to 2.6  $\mu\text{m}$  [40]. For shorter wavelengths, GaN or ZnO [41] is required and the first electrically pumped blue VCSEL (414 nm) operating at room temperature was recently demonstrated utilizing InGaN/GaN QWs [42].

---

<sup>4</sup>A single VCSEL typically measures less than  $300 \times 300 \mu\text{m}^2$ , including electrical contacts.

<sup>5</sup>The production cost of a single VCSEL used in *e.g.* computer mice is less than \$0.10.

<sup>6</sup>Honeywell is now Finisar.

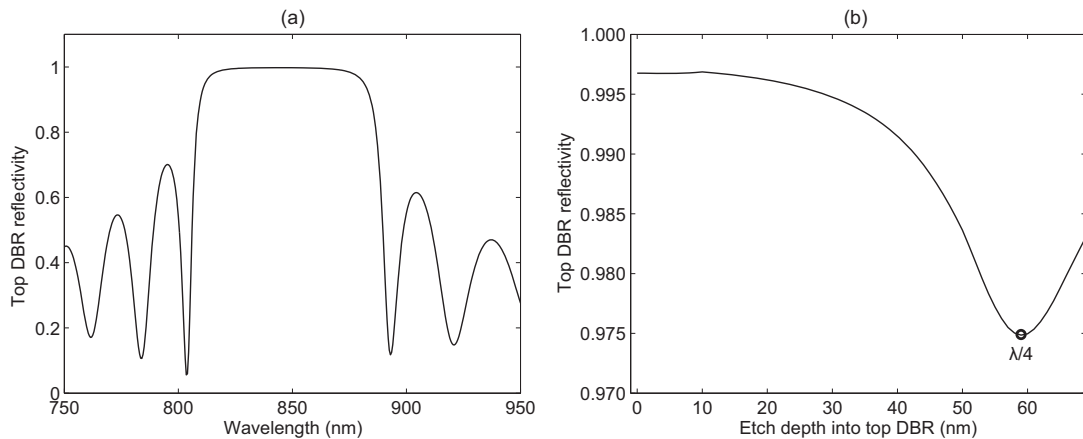


Figure 2.2: Calculated reflectivity as a function of wavelength for the top DBR used in the 850 nm VCSELs from Papers F-H containing (a) and reflectivity at center wavelength as a function of etch depth into the top DBR (b).

The optical feedback in a VCSEL is provided by DBR mirrors. These consist of multiple  $\lambda/4$  thick layers with alternating high and low refractive index and form efficient mirrors through the constructive interference experienced by the optical field when reflected at the different layer interfaces. Since the cavity is formed normal to the active region layers, the overlap between the optical field and the gain region is poor (the longitudinal confinement factor ( $\Gamma$ ) is low) and the reflectivity of the DBRs needs to be high to compensate (typically  $>99\%$  for the output DBR, and  $>99.9\%$  for the other). The highest reflectivity is obtained from mirrors with abrupt interfaces and large refractive index differences. In a conventional VCSEL, where current is injected through the mirror, this DBR design is disadvantageous since it leads to abrupt and large band discontinuities at the interfaces and results in undesirably large electrical resistance. To remedy this problem, the composition of the DBRs is often graded and clever doping schemes are employed to achieve high reflectivity and electrical conductivity simultaneously without inducing excessive free carrier absorption losses [43–45].

The number of mirror pairs required for sufficient reflectivity depend on the refractive index contrast that is possible to obtain within the material system while maintaining transparency to the laser light. For 850 nm AlGaAs VCSELs and standard  $\text{Al}_{0.12}\text{Ga}_{0.88}\text{As}/\text{Al}_{0.90}\text{Ga}_{0.10}\text{As}$  mirrors, the index difference is about  $\Delta n_{eff} = 0.5$  and  $>20$  pairs are required. Fig. 2.2 (a) shows the calculated top DBR reflectivity for the VCSEL design used in Papers F-H which utilizes this mirror scheme. Due to the large refractive index difference at the semiconductor/air interface ( $\Delta n_{eff} \approx 3.5$ ), the thickness of the top DBR layer greatly influences the total reflectivity of the mirror. By reducing the thickness of the top layer, the reflection at the semiconductor/air interface becomes increasingly out-of-phase with reflections further down in the DBR stack, resulting in a local minima of the reflectivity when  $\lambda/4$  of the mirror is removed. The effect is illus-

trated in Fig. 2.2 (b) where the reflectivity at the center wavelength is plotted as a function of etch depth into the top DBR. This phenomenon has previously been exploited to induce mode-selective loss in VCSELs and enable high single-mode power [46]. As discussed in Section 3.3.2 and illustrated in Papers F-H, the technique can also be utilized to optimize the high speed performance of the VCSEL.

Despite graded interfaces and modulation doping schemes, the DBRs remain the major contributor to electrical resistance in the VCSEL. To circumvent some of the issues related to doping and low refractive index difference in monolithic mirrors, hybrid DBR techniques have been developed where the main part of the top mirror consists of dielectric layers deposited after the epitaxial growth. High index difference can then be readily achieved, reducing the number of mirror pairs necessary for sufficient reflectivity and thereby also the effective cavity length, which can be beneficial for high speed performance. Intracavity contacts sandwiched between the doped semiconductor and dielectric mirror are used for current injection which can reduce device resistance. Impressive results with a wall-plug efficiency (WPE) as high as 62% have been demonstrated using this technique [47]. An interesting alternative to using a DBR top mirror is to use a single layer subwavelength high-index-contrast grating (HCG) reflector [48]. With this technique, the top reflector can be reduced in thickness from several micrometers for an epitaxial DBR to  $\sim 250$  nm for the HCG while, according to simulations, maintaining a reflectivity  $>99.9\%$  [49]. However, both the HCG-technique and dielectric DBRs add complexity to the fabrication process and the short distance between contact and active region makes current crowding a potential problem [50].

The short cavity formed by the DBRs in the VCSEL leads to a longitudinal mode spacing large enough for the gain spectrum to only support one longitudinal mode. This makes the VCSEL sensitive to the alignment between gain peak and cavity resonance and, contrary to the FP laser, the VCSEL emission wavelength is determined by the cavity resonance rather than the gain peak. Both the gain peak and the cavity resonance wavelengths change with increased temperature, but they change at different rates. For GaAs/AlGaAs VCSELs the gain shifts by approximately 0.32-0.33 nm/K whereas the cavity resonance shifts by approximately 0.06-0.09 nm/K [51]. The difference induces a relative shift of the laser mode and the gain spectrum with temperature. When the drive current is increased, the temperature increases accordingly and eventually, the cavity resonance and gain peak will be misaligned and the output power will drop while the threshold current increases. To reduce temperature sensitivity, the cavity resonance is often placed at the long wavelength part of the gain spectrum because an increase in temperature will then bring the gain towards the laser mode and to some extent compensate the temperature induced reduction of gain with improved mode/gain overlap. This effect of detuning is illustrated in Fig. 2.3 (a)-(d). Fig. 2.3 (e) shows the measured threshold currents as function of substrate temperature for VCSELs fabricated from the epi-material used in Papers

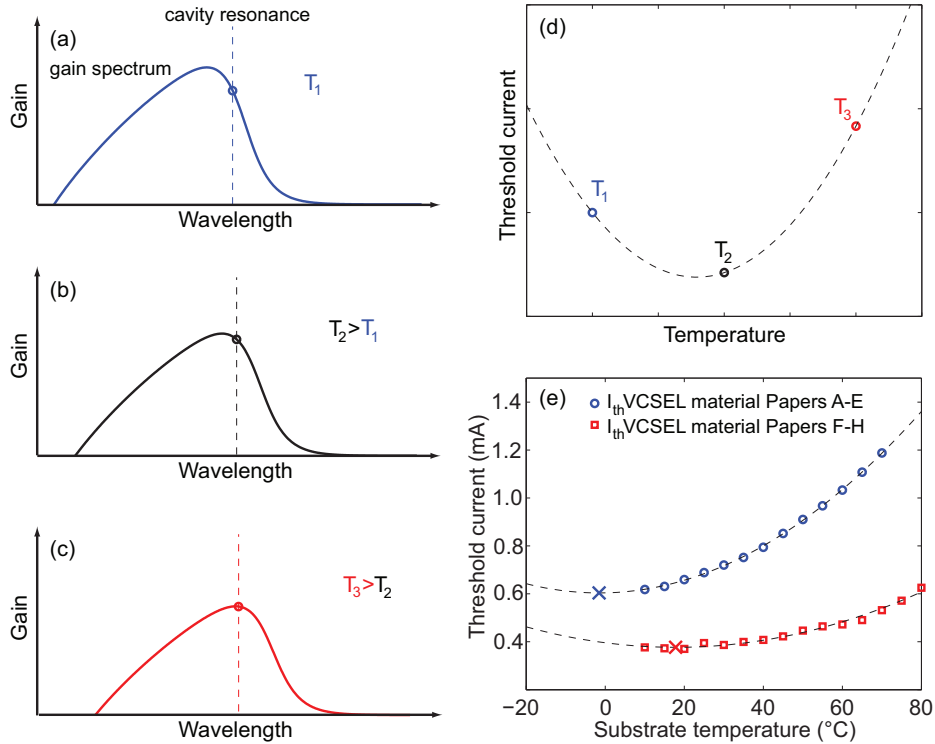


Figure 2.3: Qualitative illustration of the alignment of the cavity resonance with the gain spectrum in a VCSEL for (a) low temperature, (b) medium temperature, and (c) high temperature. (d) shows the resulting temperature dependence of the threshold current. (e) shows the threshold current measured as a function of temperature for the VCSELs in Papers A-E (circles), and Papers F-H (squares). X marks the extrapolated threshold minima.

A-H, with a characteristic parabolic dependence on temperature clearly visible. As is evident from the figure, the detuning is somewhat larger in the epi-material used in Papers F-H, resulting in a threshold minimum at higher temperature for the VCSEL fabricated from this material. The detuning of the gain peak and the cavity resonance is an important design parameter and can be used to make VCSELs that function over a wide temperature range [52, 53]. However, the increase of the VCSEL operational range comes at the price of increased threshold current at room temperature due to lower gain. Low electrical resistance, low internal absorption, and good thermal management is therefore essential to keep the device temperature from increasing too rapidly with drive current. The impact of thermal effects on the high speed properties of the VCSEL is discussed in Section 3.3.3.

## 2.2.2 Transverse confinement

Both the electrical carriers and the optical field need to be confined in order to define the transverse extent of the VCSEL cavity. Fig. 2.4 shows five confinement

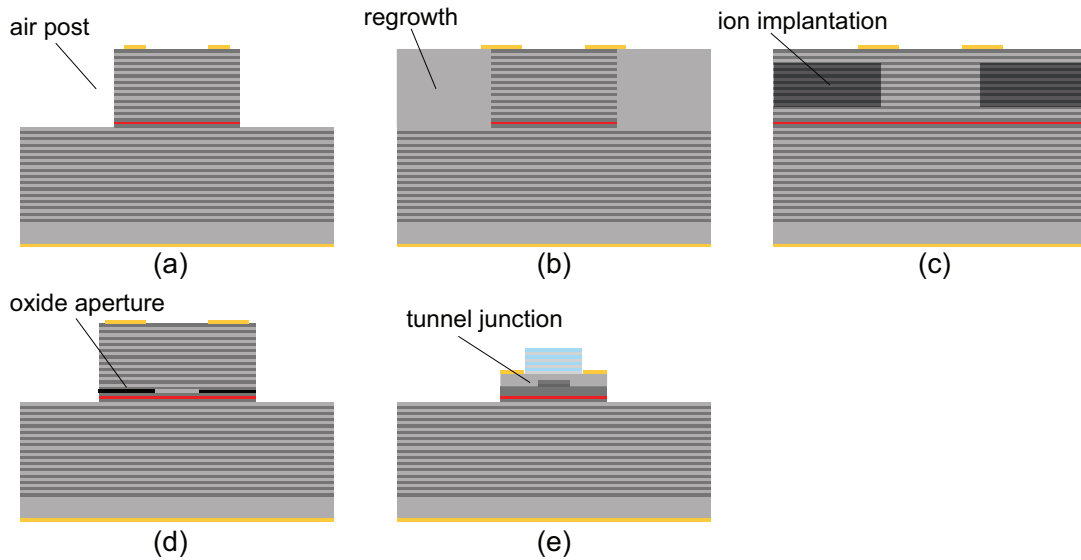


Figure 2.4: Different VCSEL designs, (a) etched air-post, (b) regrown buried mesa, (c) ion-implanted, (d) oxide confined, and (e) buried tunnel junction (BTJ).

schemes: the etched air-post, the regrown buried mesa, the ion-implanted, the oxide confined, and the buried tunnel junction VCSEL structure. Early VCSELs<sup>7</sup> used the simple etched air-post structure shown in Fig. 2.4 (a) where the large refractive index difference at the semiconductor/air interface results in a strong index guiding of the optical field. However, the confinement technique is not ideal since it suffers from issues with *e.g.* diffraction loss, surface recombination, and thermal management. A development from this basic structure is the regrown buried mesa VCSEL shown in Fig. 2.4 (b). Here, a new semiconductor material with a higher bandgap (lower refractive index) is grown on top of the air-post structure, thereby reducing or eliminating many of the problem associated with the semiconductor/air interface. However, this technique is complex and particularly challenging in AlGaAs based short wavelength systems since the Al-content layers exposed after etching the mesa are highly reactive to the atmosphere.

The ion-implanted structure illustrated in Fig. 2.4 (c) has rendered more success than the previously mentioned techniques. This is the confinement scheme that was used in the first commercial VCSELs due to relatively simple fabrication and excellent device life-time and reliability [55]. By selectively implanting ions into the semiconductor material, it can be rendered electrically isolating and the flow of the injected current can be controlled. Different ion species have been used, but protons ( $H^+$ ) is the most common choice. The proton implant confines the current, but it does not provide any inherent index guiding of the optical field. Instead, optical confinement is provided by gain guiding and thermal lensing (the temperature rise associated with the drive current produces a

<sup>7</sup>For example the first monolithic, electrically pumped VCSEL [54].

refractive index difference which gives rise to index guiding of the optical mode). However, this guiding is relatively weak and results in drive current dependent mode behavior [56].

A clever confinement method possible in GaAs based systems is to form an oxide aperture as shown in Fig. 2.4 (d). By including a high Al-content layer ( $\sim 98\%$  Al) in the DBR structure during the epitaxial growth, a selectively oxidized aperture can be formed in subsequent processing steps. After a mesa is etched to expose the high Al-content layer, the wafer is put into an oxidation furnace with a steam atmosphere at  $\sim 400^\circ\text{C}$ . This converts the AlGaAs to a robust insulating oxide with a lower refractive index than the rest of the mesa. Since the oxidation rate is highly dependent on Al-concentration, the oxide aperture will basically be formed only by the highest Al-content layers. This confinement approach offers a lot of freedom in the design of the transverse confinement as placement, size, and the number of apertures can be varied. Multiple oxide apertures can be beneficial in high speed applications, as discussed in Section 3.3.4, but the conventional scheme is to include a single oxide aperture placed close to the active region to ensure uniform current injection and minimal loss of carriers due to diffusion. Compared to ion-implantation, the oxide confinement technique offers better optical mode and gain overlap, which results in VCSELs with lower threshold currents, higher differential efficiency, and more linear current-power relationship. Ever since high reliability was proven feasible in oxide aperture VCSELs [57], the use of ion-implantation has been phased out and today oxide confinement is the de facto standard confinement method for GaAs VCSELs. A disadvantage with the oxide confined design is the difficulty to produce apertures of a predetermined size. This is due to the extreme sensitivity in AlGaAs oxidation rate on Al-composition and layer thickness, and growth variations of a few % in these parameters over a wafer can cause significantly different aperture sizes. This problem is particularly pronounced when aiming for small aperture sizes (a few  $\mu\text{m}$ ), and as a consequence, commercial oxide confined VCSELs typically have aperture diameters  $\geq 10\ \mu\text{m}$  leading to multimode operation. The use of relatively large apertures in commercial VCSELs also stems from reliability issues since small aperture leads to high current densities and greater sensitivity to ESD damage which can lead to premature device failure [57].

Both electrical and optical confinement can be provided using a buried tunnel junction (BTJ) as shown in Fig. 2.4 (e). Carrier confinement arises from the fact that the  $n/p$  interfaces at the side of the BTJ function as a reverse biased diode when the VCSEL is forward biased. This leads to an effective confinement of the current to the BTJ area and to the active region just next to it. The BTJ has wider bandgap than the QWs to avoid band-to-band absorption. The refractive index step from the BTJ and the surrounding cladding material propagates through the VCSEL structure during growth and gives rise to index guiding of the optical field. With a BTJ, it is possible to use mostly  $n$ -doped material in the VCSEL (except for a thin layer of  $p$ -doping next to the junction) which can reduce electrical resistance and free carrier absorption significantly. Combined

with dielectric mirrors, this confinement technique has been particularly successful in InP-based, long wavelength VCSELs [58, 59] since this material system otherwise suffers from drawbacks such as low thermal conductivity, high temperature sensitivity, and low index contrast in the epitaxial mirrors [60]. However, the fabrication process for a BTJ VCSEL is rather complex since it requires a regrowth step and due to the success of oxide confinement in GaAs-based VCSELs and to problems of finding suitable materials to produce low resistance junctions while maintaining low optical absorption, short wavelength VCSELs with a BTJ have not rendered much success [61]. Today, the technique is therefore mainly used in InP-based or GaSb-based devices with emission wavelengths  $>1.3\mu\text{m}$ , although high performance GaAs-based BTJ VCSELs have been demonstrated around 1100 nm [21, 62].

# 3 Dynamic VCSEL properties

The research presented in Papers A-H has been concerned with optimizing the dynamic properties of oxide confined VCSELs operating in multiple transverse modes. To understand the dynamic behavior of the photon-carrier interaction in a VCSEL biased above threshold, one usually resort to studying rate equations.

## 3.1 Rate equations

The common method for analyzing the intrinsic dynamic behavior of semiconductor lasers begins with formulating a set of two coupled rate equations; one for the carrier density in the active region<sup>1</sup>, and one for the photon density of the lasing mode in the cavity. For a multimode laser (such as the VCSELs in Papers A-H), one generally needs to extend these equations so that each lasing mode is represented. However, it has been shown that as long as the total output power is considered, the dynamic behavior of index guided multimode VCSELs with highly overlapping transverse intensity fields (such as oxide confined devices) have uniform transverse carrier and photon densities and exhibit a single resonance frequency very similar to that of a single mode VCSEL [63,64]. Therefore, single mode rate equations analysis can be used to describe and understand the intrinsic dynamic modulation behavior of these VCSELs. The finite rate at which carriers are captured into the QWs from the SCH can cause a parasitic-like roll-off in the frequency response and should be accounted for in the general case. These effects can be included in the rate equation formalism by treating the carriers in the active region separately from the carriers in the SCH and formulate three equations rather than two [65]. However, the VCSEL design employed in Papers A-H has a narrow, graded SCH and effects from carrier transport can be considered negligible [65]. We are consequently comfortable with using the "standard" two rate equations and following Coldren and Corzine [66], these can be written as:

$$\frac{dN}{dt} = \frac{\eta_i I}{qV_a} - (AN + BN^2 + CN^3) - v_g GS, \quad (3.1)$$

$$\frac{dS}{dt} = \Gamma v_g GS - \frac{S}{\tau_p} + \Gamma \beta BN^2, \quad (3.2)$$

---

<sup>1</sup>For an undoped active region at the high injection levels relevant for lasers, charge neutrality requires the density of electrons and holes to be equal. Consequently, it is sufficient to formulate an equation for only one type of carrier.

where  $N$  is the excess carrier density in the active region,  $\eta_i$  the internal quantum efficiency<sup>2</sup>,  $I$  is the injected current,  $q$  is the elementary charge,  $AN + BN^2 + CN^3$  is the recombination rate from spontaneous and non-radiative recombination<sup>3</sup>,  $v_g$  is the group velocity of the lasing mode,  $G$  the material gain,  $S$  the photon density of the lasing mode,  $\tau_p$  is the photon lifetime which is related to the cavity losses through  $\tau_p^{-1} = v_g \cdot [\alpha_i + \alpha_m]$ , and  $\beta$  is the fraction of photons generated by spontaneous emission which goes into the lasing mode.

In order to incorporate the phenomenological fact that gain is compressed at high photon densities, we write  $G$  as [67]:

$$G = G(N, S) = \frac{g(N)}{1 + \varepsilon S}, \quad (3.3)$$

where  $\varepsilon$  is referred to as the gain compression factor and accounts for the non-linear effects caused mainly by spectral hole-burning and carrier heating [68].

Unfortunately, exact analytical solutions to the rate equations away from steady-state (with the time derivatives  $\neq 0$ ) do not exist. However, if we make the approximation that perturbations away from steady-state are small, we can proceed with the analysis.

## 3.2 Small signal modulation

To investigate the small signal response of Eqs. 3.1 and 3.2 of one variable in terms of a perturbation of another, we make a Taylor expansion to the first order and the following substitutions:  $I = I_b + \delta I$ ,  $N = N_b + \delta N$ ,  $S = S_b + \delta S$ , and  $G(N, S) = g_b/(1 + \varepsilon S) + g_0 \delta N/(1 + \varepsilon S) - \varepsilon G \delta S/(1 + \varepsilon S)$ . The subscript  $b$  denotes that we are linearizing around some biasing point  $I_b$  above threshold. Note that gain clamps at threshold and therefore  $g_b$  is identical to the threshold gain  $g_{th}$  from Eq. 2.1 (where gain compression was neglected).  $g_0$  is the nominal differential gain  $\partial g/\partial N$  at the biasing point, *i.e.* the differential gain without gain compression. Neglecting higher order terms and setting the time derivatives of the steady-state quantities to zero, the resulting small signal equations become:

$$\frac{d}{dt} \delta N = \frac{\eta_i}{qV_a} \delta I - \left[ \frac{1}{\tau_{\Delta N}} + \frac{v_g g_0 S_b}{1 + \varepsilon S_b} \right] \delta N - \left[ \frac{1}{\Gamma \tau_p} - \frac{v_g \varepsilon G S_b}{1 + \varepsilon S_b} \right] \delta S, \quad (3.4)$$

$$\frac{d}{dt} \delta S = \frac{\Gamma v_g g_0 S_b}{1 + \varepsilon S_b} \delta N - \frac{\Gamma v_g \varepsilon G S_b}{1 + \varepsilon S_b} \delta S, \quad (3.5)$$

where  $1/\tau_{\Delta N} = A + 2BN_b + 3CN_b^2$  and  $\tau_{\Delta N}$  is the differential carrier lifetime and we have made use of the steady-state relation  $1/\Gamma \tau_p = v_g g_b/(1 + \varepsilon S_b)$ . The spontaneous emission factor ( $\beta$ ) term is neglected since it only has an impact

<sup>2</sup> $\eta_i$  is defined as the fraction of injected current that generates carriers in the active region.

<sup>3</sup> $A$  is the Shockley-Read-Hall recombination coefficient,  $B$  the spontaneous emission coefficient, and  $C$  the Auger recombination coefficient.

at low power levels where it contributes to additional damping [69]. By taking the time derivative of Eq. 3.5 and plugging it into Eq. 3.4 to eliminate  $\delta N$ , we recognize a second order system:

$$\frac{d^2}{dt^2} \delta S + \gamma \frac{d}{dt} \delta S + 4\pi^2 f_r^2 \delta S = \frac{\eta_i}{qV_a} \frac{\Gamma v_g g_0 S_b}{1 + \varepsilon S_b} \delta I, \quad (3.6)$$

where the resonance frequency ( $f_r$ ) and the damping factor ( $\gamma$ ) can be written as

$$f_r^2 = \frac{1}{4\pi^2} \left[ \frac{1}{\tau_p} \frac{v_g g_0 S_b}{1 + \varepsilon S_b} + \frac{1}{\tau_{\Delta N}} \frac{\Gamma v_g \varepsilon G S_b}{1 + \varepsilon S_b} \right], \quad (3.7)$$

$$\gamma = \frac{v_g g_0 S_b}{1 + \varepsilon S_b} + \frac{\Gamma v_g \varepsilon G S_b}{1 + \varepsilon S_b} + \frac{1}{\tau_{\Delta N}}. \quad (3.8)$$

To link Eq. 3.6 to a measurable quantity, we first connect the photon density to the optical output power via  $P_{out} = \eta_o hc S V_p / \lambda_0 \tau_p$ , where  $\eta_o$  is the optical efficiency<sup>4</sup> and  $V_p$  the volume of the lasing mode. In order to find the modulation response to a small sinusoidal current change  $\delta I(t) = \delta I_0 e^{j2\pi f t}$ , we substitute  $d/dt$  with  $j2\pi f$  in Eq. 3.6. With  $\delta S(t) = \delta S_0 e^{j2\pi f t}$  and  $\delta P_{out}(t) = \delta P_0 e^{j2\pi f t}$ , this procedure results in an expression for the transfer function  $H_i(f)$  for the intrinsic modulation response as:

$$H_i(f) = \frac{\delta P_0}{\delta I_0} = \eta_d \frac{hc}{\lambda_0 q} \cdot \frac{f_r^2}{f_r^2 - f^2 + j \frac{f}{2\pi} \gamma}, \quad (3.9)$$

where  $\eta_d = \eta_i \eta_o$  is the differential quantum efficiency and we have used an approximate expression for  $f_r$ ,

$$f_r \approx \frac{1}{2\pi} \sqrt{\frac{v_g g_0 S_b}{\tau_p (1 + \varepsilon S_b)}}, \quad (3.10)$$

obtained by considering that  $\tau_p \ll \tau_{\Delta N}$  and  $g_0 \sim \Gamma \varepsilon G$  [66]. Using Eq. 3.10 we can rewrite the damping factor as

$$\gamma \approx K \cdot f_r^2 + \gamma_0 \quad \text{with} \quad K = 4\pi^2 \left[ \tau_p + \frac{\varepsilon}{v_g g_0} \right], \quad (3.11)$$

where  $\gamma_0 = 1/\tau_{\Delta N}$  is the damping factor offset and  $K$  is the so-called  $K$ -factor. Eqs. 3.10 and 3.11 illustrate the intrinsic damping limitation of the laser system. As the photon density is increased (by increasing the injection current), the resonance frequency increases as  $f_r \propto \sqrt{S_b}$ . However, since  $\gamma \propto f_r^2 \propto S_b$ , the damping of the system increases at a faster pace and will eventually limit the modulation bandwidth, *i.e.* even if  $S_b$  could be increased to arbitrarily high levels without detrimental effects from device heating, damping would still limit the

---

<sup>4</sup> $\eta_o$  is defined as the fraction of the optical field that couples out from the cavity.

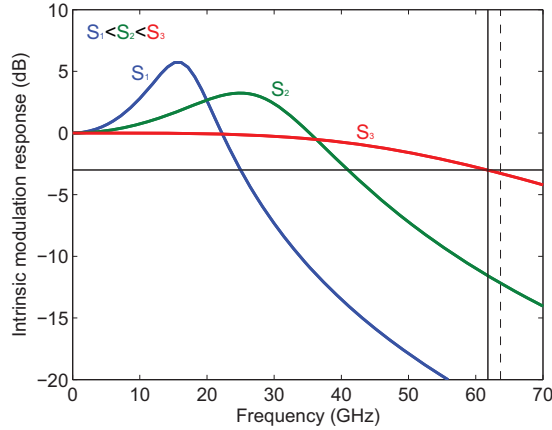


Figure 3.1: Intrinsic modulation response ( $20 \log |H_i(f)/H_i(0)|$ ) for increasing photon densities calculated using  $K = 0.14 \text{ ns}$  and  $\gamma_0 = 16.8 \text{ ns}^{-1}$  as extrapolated from one of the VCSELs of Paper H.  $-3\text{dB}$  and  $f_{3\text{dB},\text{max}} = 2\sqrt{2}\pi/K - \gamma_0/2\sqrt{2}\pi$  (solid) as well as  $f_{3\text{dB},\text{max}} = 2\sqrt{2}\pi/K$  (dashed) are also shown, illustrating the overestimation of  $f_{3\text{dB},\text{max}}$  when using the latter approximation while  $\gamma_0 \neq 0$ .

maximum bandwidth. The maximum achievable intrinsic 3dB bandwidth<sup>5</sup> in a semiconductor laser ( $f_{3\text{dB},\text{max}}$ ) is therefore set by the  $K$ -factor and  $\gamma_0$ . The limit can be found by considering that at  $f_{3\text{dB},\text{max}}$ ,  $|H_i(f_{3\text{dB},\text{max}})|^2/|H_i(0)|^2 = 1/2$  and  $d(|H_i(f_{3\text{dB},\text{max}})|^2)/d(f_r^2) = 0$ . Solving this equation system yields

$$f_{3\text{dB},\text{max}} \approx \frac{2\sqrt{2}\pi}{K} - \frac{\gamma_0}{2\sqrt{2}\pi}. \quad (3.12)$$

This expression differs from the commonly used  $f_{3\text{dB},\text{max}} \approx 2\sqrt{2}\pi/K$  as derived by Olshansky *et al.* [70] which overestimates  $f_{3\text{dB},\text{max}}$  since it neglects  $\gamma_0$ . Fig. 3.1 shows the behavior of  $|H_i(f)|^2$  for increasing photon densities using values for  $K$  and  $\gamma_0$  obtained for a VCSEL in Paper H ( $K = 0.14 \text{ ns}$  and  $\gamma_0 = 16.8 \text{ ns}^{-1}$ ). As seen in the figure, the maximum intrinsic bandwidth for this device exceeds 60 GHz. Indeed,  $f_{3\text{dB},\text{max}} > 30 \text{ GHz}$  is not uncommon for VCSELs [71]. As discussed further in Section 3.3, however, extrinsic effects from self-heating and electrical parasitics tend to reduce the maximum bandwidth significantly and the damping limit is therefore seldom reached. For the VCSEL in Fig. 3.1, the measured maximum 3dB bandwidth is approximately 20 GHz.

For actual devices, the so-called  $D$ -factor is an important figure of merit quantifying the rate at which the resonance frequency increases with current. It is defined as:

$$D \equiv \frac{f_r}{\sqrt{I_b - I_{th}}} = \frac{1}{2\pi} \sqrt{\frac{\eta_i \Gamma v_g g_0}{q V_a}}, \quad (3.13)$$

<sup>5</sup>The intrinsic 3dB bandwidth  $f_{3\text{dB}}$  is defined as  $|H_i(f_{3\text{dB}})|^2/|H_i(0)|^2 = 1/2$ .

where  $I_{th}$  is the threshold current and the relation  $S_b V_p / \tau_p = S_b V_a / \Gamma \tau_p = \eta_i (I_b - I_{th}) / q$  has been used. Note that the gain compression term from Eq. 3.10 is dropped in Eq. 3.13. There is indeed a saturation of the resonance frequency at high currents in VCSELs, but as discussed in Section 3.3.3, this is mainly due to self-heating effects and not caused by gain compression. Due to this saturation, the  $D$ -factor is always evaluated at low currents (and consequently low photon densities), where the relation  $f_r \propto \sqrt{I_b - I_{th}}$  holds since both thermal effects and effects from gain compression on differential gain are negligible ( $\varepsilon S_b \ll 1$ ). If all other parameters are known, Eq. 3.13 can therefore be used to extract the nominal differential gain from modulation response measurements (as is done in Papers E and H).

It should be noted here that had effects from carrier transport been included in the analysis, an additional pole would have appeared in the transfer function  $H_i(f)$  due to the finite capture time from the SCH to the QWs. Furthermore, the nominal differential gain  $g_0$  and the damping factor offset  $\gamma_0$  would have been reduced to  $g_0/\chi$  and  $\gamma_0/\chi$ , respectively. The term  $\chi$  is referred to as the transport factor and is related to the carrier transport time across the SCH to the QWs ( $\tau_s$ ) and the escape time of carriers from the QWs into the barrier and SCH layers ( $\tau_e$ ) through  $\chi = 1 + \tau_s/\tau_e$  [65]. If  $\chi$  is not considered in the design of the SCH, the effects from carrier transport can hamper the modulation response significantly. However, in our VCSEL structure design,  $\tau_s \ll \tau_e$  and  $\chi \approx 1$  and, as mentioned before, transport effects are considered to be negligible.

### 3.3 High speed VCSEL design

With the expressions derived for the resonance frequency and the  $K$ -factor in Section 3.2 it is clear that certain device parameters play a crucial roll in determining the dynamic limitations of the VCSEL. As was also mentioned, the intrinsic damping limit is typically beyond the actual, measured maximum bandwidth. This is because, in addition to the intrinsic limitations, performance limiting factors in VCSELs arise from device heating and electrical parasitics. Consequently, the performance is limited by a combination of all these effects, and they all need to be carefully considered when designing the component. Fig. 3.2 shows the calculated modulation response after effects from electrical parasitics (a) and electrical parasitics and self-heating (d) have been added to the intrinsic response from Fig. 3.1, again using parameters extracted from the VCSEL in Paper H. Clearly, electrical parasitics and thermal effects influence the maximum bandwidth and the following points need to be addressed when designing the VCSEL for high speed applications:

- The active region must provide high differential gain
- Damping must be suppressed
- Thermal impedance needs to be low and heat generation suppressed

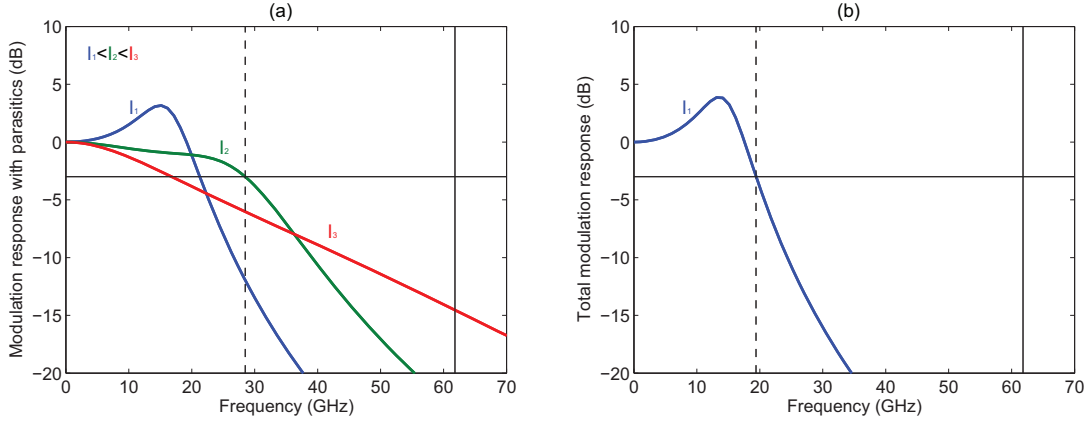


Figure 3.2: Small signal modulation response at increasing bias currents calculated using  $K = 0.14 \text{ ns}$ ,  $\gamma_0 = 16.8 \text{ ns}^{-1}$ ,  $D = 4.44 \text{ GHz}/\sqrt{\text{mA}}$ , a parasitic pole at  $f_p = 17 \text{ GHz}$ , and  $f_{r,max} \approx 15 \text{ GHz}$  as derived from one of the VCSELs of Paper H. The bias currents correspond to the photon densities from Fig. 3.1 ( $I_b \leftrightarrow S_b$ ). (a) shows the intrinsic response with added effects from electrical parasitics, resulting in a reduction of  $f_{3dB,max}$  to  $\sim 30 \text{ GHz}$  at  $I_2 \approx 45 \text{ mA}$  and (b) is the total response, taking intrinsic effects, parasitics, and the thermal saturation of  $f_r$  into account. The resulting curve corresponds to the measured maximum bandwidth modulation response from Paper H with  $f_{3dB,max} \sim 20 \text{ GHz}$  at  $I_1 \approx 15 \text{ mA}$ .  $I_2$  and  $I_3$  are now beyond the point of thermal saturation.

- Parasitic capacitance and electrical resistance need to be minimized

It is important to emphasize that the bandwidth is rarely limited by the single effect of either damping, self-heating, or electrical parasitics, but by a combination of them all. Additionally, as *e.g.* damping and resonance frequency are interrelated ( $g_0$  is included in both the  $K$ - and  $D$ -factor and is also affected by  $\tau_p$ ), design trade-offs are required for optimized performance.

Two generation VCSEL structures were developed for this work with the above mentioned design points in mind. The Gen I devices, containing two versions with different active region designs, were used in Papers A-E and evolved into the Gen II design used in Papers F-H. Fig. 3.3 shows a schematic illustration of the VCSEL structures, with the various design features indicated.

### 3.3.1 Active region

In order to approach the damping limited modulation bandwidth at low injection currents and before thermal degradation sets in, it is crucial that the resonance frequency increases at a high rate with current. This translates to a requirement that the  $D$ -factor from Eq. 3.13 should be as large as possible which is facilitated by a high differential gain ( $g_0$ ). One method of increasing the differential gain (and also of reducing the threshold carrier density) is to use strained QWs and in

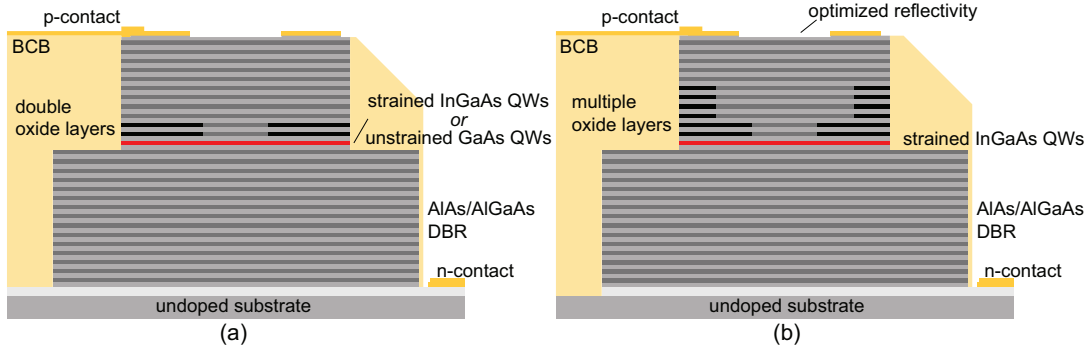


Figure 3.3: Schematic view of the high speed VCSEL designs used for this work. (a) is the structure used in Papers A-E (Gen I) which evolved into (b), the design in Papers F-H (Gen II). The various design features are indicated.

the GaAs system, compressive strain can be attained by using  $\text{In}_x\text{Ga}_{1-x}\text{As}$  as the gain material [72]. However, in addition to increased strain with increased In content, the gain peak also shifts to longer wavelengths due to smaller bandgap. This is part of the reason why some of the most impressive high speed VCSEL results have been achieved at wavelengths of 980 nm [17, 18] and around 1100 nm [21] where heavily strained InGaAs/AlGaAs QWs can be utilized, resulting in lower threshold carrier density and higher differential gain and therefore increased  $D$ -factor [73, 74]. In conventional designs for emission at 850 nm, the active region consists of unstrained GaAs QWs which provide moderate differential gain. In Paper B, we show that by replacing the GaAs/AlGaAs QWs with strained InGaAs/AlGaAs QWs while compensating with reduced QW width and increased Al-content in the barriers to maintain a gain peak close to 850 nm, it is possible to increase the  $D$ -factor by more than 50%. This enhancement pushed the maximum modulation bandwidth from 16.5 GHz to 20.0 GHz in a 9  $\mu\text{m}$  aperture 850 nm VCSEL and, as shown in Paper C, allowed for error-free transmission at data rates up to 32 Gbit/s. The improvement is further investigated in Paper E where gain calculations are used to confirm that the experimental findings are indeed due to a strain-induced increase of the differential gain.

The fact that the lasing wavelength is determined by the cavity resonance in a VCSEL can in principle be utilized to further improve  $g_0$ . Differential gain is highest at the short wavelength side of the gain spectrum [69] and this effect has previously been exploited in DFB lasers to improve the  $D$ -factor and the modulation bandwidth [75]. However, considering that VCSELs are prone to self-heating, this enhancement technique is not practical since it will lead to premature thermal degradation and reduce the operational range unless *e.g.* thermoelectric cooling is used. Another way of improving differential gain is by  $p$ -type doping of the active region [66]. However, the improvement comes at the expense of increased internal absorption losses and consequently higher threshold carrier density. Again, this trade-off may not be practical in VCSELs due to the necessity of keeping operating currents and absorption at a minimum

to minimize self-heating.

Tight confinement of the optical mode to the active region (high  $\Gamma$ ) is also important for a high  $D$ -factor. VCSELs have inherently low confinement in the longitudinal direction since the cavity is formed normal to the thin active region layers ( $\Gamma$  is typically only a few % in a  $1\lambda$  cavity VCSEL). In principle, the confinement factor can be increased by increasing the length of the SCH to multiple  $\lambda$  and adding QWs at each antinode of the optical field. However, this approach also increases the active volume  $V_a$  and consequently the change in  $V_a/\Gamma = V_p$  may be small. Furthermore, this method is not practical for high speed VCSELs as effects from carrier transport over the resulting, long SCH region would deteriorate the dynamic performance. Replacing the DBRs with HCG reflectors (or high contrast dielectric DBRs) is an approach that can be used to compress the longitudinal field and improve optical confinement without increasing  $V_a$ . However, the effective cavity length when using epitaxial DBRs is already short in the GaAs system (the effective penetration depth of the optical field into the DBR is typically  $<1\mu\text{m}$  even though the DBR is several microns thick). Since current spreading layers are needed between the reflector and the active region for efficient carrier injection, the resulting improvement in confinement might be limited.

### 3.3.2 Damping

Despite the fact that the damping limit may be difficult to reach, low damping is essential for high speed performance. In combination with limiting effects from electrical parasitics for example, the high resonance peak of the modulation response associated with low damping can help push the bandwidth to a higher frequency. Low damping translates to a requirement of a low  $K$ -factor and from Eq. 3.11 we recognize that this is facilitated by a short photon lifetime, low gain compression, and high differential gain.

If the  $K$ -factor is limited by the photon lifetime, as is often the case for high- $Q$  cavity VCSELs, reducing  $\tau_p$  is an efficient way of reducing  $K$ . In Section 2.2.1 we mentioned that the top mirror reflectivity (and therefore loss) can be greatly influenced by a shallow etch into the top DBR. Since  $\tau_p^{-1} = v_g \cdot [\alpha_i + \alpha_m]$ , this means that the photon lifetime is affected by the procedure as well. Fig. 3.4 shows the photon lifetime calculated at the center wavelength for the Gen II VCSEL structure from Papers F-H as a function of etch depth into the top DBR. As is also shown in the figure, the same effect can be realized by applying an AR-coating on top of the DBR. The lowest attainable  $\tau_p$  is determined by the refractive index step at the resulting semiconductor/air (or dielectric/air) interface. In Paper F, we use the shallow etch technique to optimize  $\tau_p$  and the  $K$ -factor and improve the maximum modulation bandwidth by more than 50% when reducing  $\tau_p$  from 6.4 to 3.3 ps, reaching a modulation bandwidth of 23 GHz for a  $7\mu\text{m}$  aperture 850 nm VCSEL. In Paper G, the same VCSEL enables error-free transmission at data rates up to 40 Gbit/s. These results demonstrate the importance of a

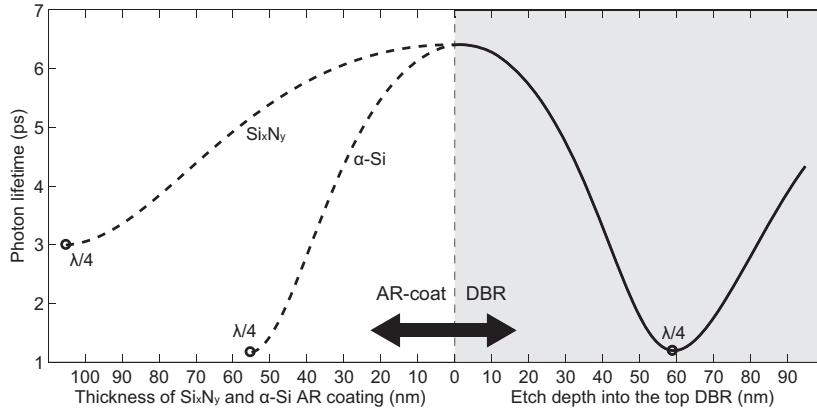


Figure 3.4: Photon lifetime for the center wavelength as function of  $\text{Si}_x\text{N}_y$  and  $\alpha\text{-Si}$  thickness (dashed) and etch depth into the top DBR (solid) calculated for the VCSEL structure from Papers F-H.

low  $\tau_p$ . However, due to the increased losses associated with a lower photon lifetime, the threshold current increases with reduced  $\tau_p$ , resulting in an increase of the carrier density and therefore a reduction of the differential gain and the  $D$ -factor. Additionally, since  $\gamma_0$  is proportional to the carrier density, the damping factor offset also increases with increased mirror loss. There is consequently an important trade-off to consider when optimizing  $\tau_p$ . This is explored in Paper H, where the optimum photon lifetime in our Gen II VCSEL design is determined to be approximately  $\tau_p \approx 3$  ps, corresponding to a  $\sim 40$  nm etch into the top DBR. Obviously, if the optimum  $\tau_p$  is known when designing the VCSEL structure, the DBR can be made to provide the corresponding reflectivity already after the epitaxial growth of the structure, making the etch/AR-coat processing step redundant.

Considering the  $\varepsilon/g_0$ -term in the expression for the  $K$ -factor, we see that high differential gain is not only beneficial for a high  $D$ -factor, but also for lowering the damping. While the thermal saturation of  $S_b$  leads to  $\varepsilon$  not having a significant impact on the maximum resonance frequency, gain compression is of importance for the  $K$ -factor and should be kept as low as possible. In addition to improved carrier transport properties, an SCH region optimized for a short carrier capture time  $\tau_s$  has also been shown to reduce  $\varepsilon$  and thus the  $K$ -factor [76]. In DFB-lasers,  $p$ -doping of the active region is another approach that has been attributed to lower  $\varepsilon$  (in addition to improving  $g_0$ ) through reduced intraband relaxation times and an associated reduction of the impact from spectral hole burning on gain compression [74]. For VCSELs with non-uniform optical fields (*e.g.* single mode VCSELs), effects from spatial hole burning can add to the gain suppression and increase damping [77]. This problem can be mitigated by using a VCSEL with a tapered oxide aperture to provide an electrical aperture that is smaller than the optical aperture and thus confine the current more tightly to the peak region of the optical mode [78, 79].

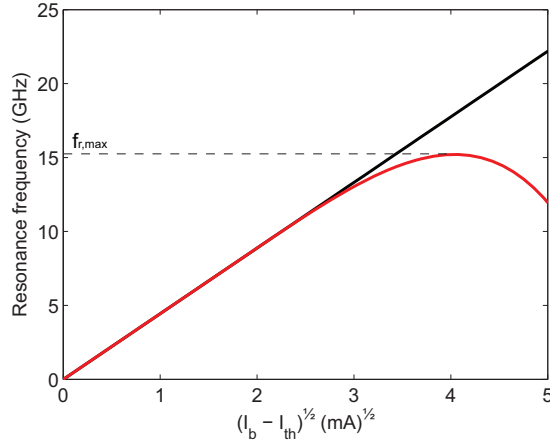


Figure 3.5: The resonance frequency plotted against  $\sqrt{I_b - I_{th}}$ , without effects from thermal saturation (black) and with saturation due to self-heating (red), calculated using  $D = 4.44 \text{ GHz}/\sqrt{\text{mA}}$  and  $f_{r,max} \approx 15 \text{ GHz}$  (indicated) as extrapolated from one of the VCSELs of Paper H.

### 3.3.3 Thermal effects

Because the resonance frequency increases with current as  $\sqrt{I_b - I_{th}}$ , the laser must be biased at several times  $I_{th}$  to reach the photon densities required for high modulation bandwidths. However, as the current is increased, self-heating causes an associated increase of the internal device temperature. Contributions come from various sources such as Joule heating from power dissipated in the resistive elements of the VCSEL, non-radiative recombination, carrier thermalization due to power lost in various scattering mechanisms [80], leakage currents, and internal absorption of the optical field. Eventually, the output power (and photon density) begins to saturate and at some point even reduces with a further increase of current. This marks the thermal rollover point in the current-power characteristics and, since  $f_r \propto \sqrt{S_b}$ , results in an accompanying saturation of the resonance frequency as illustrated in Fig. 3.5, once again using parameters extracted from the VCSEL in Paper H. An increase in temperature also influences the various dynamic parameters included in the expressions for the  $D$ - and  $K$ -factors. For example, differential gain is reduced with temperature due to reduced gain and increased carrier density (which is due both to increased leakage currents (reduced  $\eta_i$ ) and an increase of the pump level required to reach threshold with lower gain). If the resonance peak is detuned to the long wavelength side of the gain spectrum, this effect can, to an extent, be compensated by the temperature induced change in detuning towards shorter wavelengths (which increases  $g_0$ ). The damping factor offset increases with temperature because of increased threshold carrier density, but the  $K$ -factor is relatively temperature stable (see *e.g.* [81], Paper B and Paper H). Free carrier absorption ( $\alpha_{fc}$ ) increases with temperature due to increased phonon scattering rates and a related decrease of the carrier relaxation times [82]. This leads to a reduction of  $\tau_p$  and,

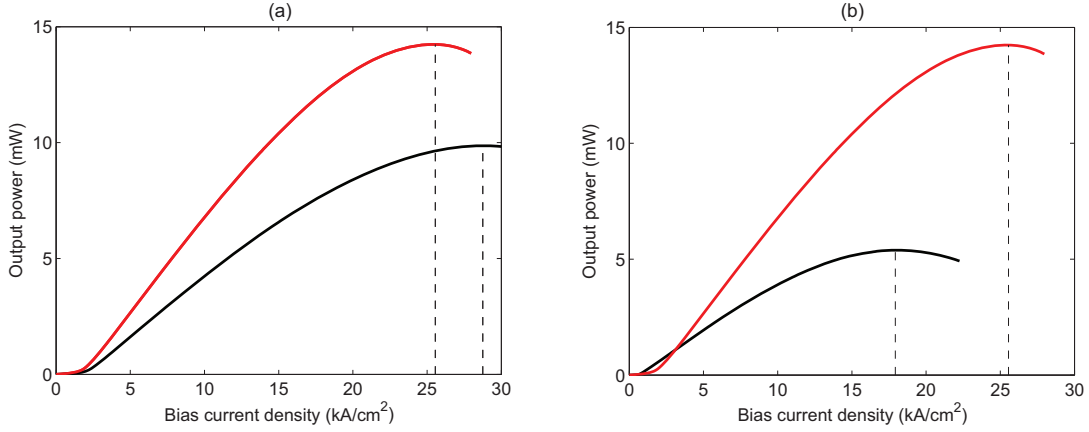


Figure 3.6: (a) Measured current density–power characteristics for an 11  $\mu\text{m}$  (red) and a 9  $\mu\text{m}$  Gen II VCSEL (black), both with  $\alpha_m^T = 0.66 \text{ ps}^{-1}$  and (b) for two 11  $\mu\text{m}$  Gen II VCSELs with  $\alpha_m^T = 0.06 \text{ ps}^{-1}$  (black) and  $\alpha_m^T = 0.66 \text{ ps}^{-1}$  (red).

combined with the reduction of  $g_0$ , results in a temperature insensitive  $K$ -factor. Nonetheless, in order to delay overall performance degradation, all heat sources need to be minimized.

The temperature increase ( $\Delta T$ ) for a given power dissipation ( $P_{diss}$ ) can be quantified via the thermal impedance  $R_{th}$  as  $\Delta T = R_{th} \cdot P_{diss}$ . For a cylindrical, oxide confined VCSEL on a thick substrate, an approximate analytical expression for the thermal impedance can be written as  $R_{th} = 1/2\xi d$  [66], where  $\xi$  is the effective thermal conductivity of the VCSEL material (assumed isotropic) and  $d$  approximately corresponds to the aperture diameter. If we make a simplification and assume that the major contribution to  $\Delta T$  comes from resistive Joule heating via the VCSEL resistance  $R$ , the dissipated power can be expressed as  $P_{diss} = I_b^2 \cdot R$ . Further assuming that  $R \propto 1/d^2$ , the temperature increase can be rewritten as  $\Delta T \propto J_b^2 \cdot d$ , where  $J_b$  is the bias current density. From this simplistic derivation, we note that under these assumptions, the temperature increase at a given current density is proportional to the aperture diameter, *i.e.* smaller diameter VCSELs can operate at higher current densities before they reach thermal rollover. This is illustrated in Fig. 3.6 (a), where the output power is plotted vs. current density for an 11  $\mu\text{m}$  and a 9  $\mu\text{m}$  Gen II VCSEL, both with mirror loss rates of  $0.66 \text{ ps}^{-1}$ . This delay in thermal rollover is part of the reason behind why smaller aperture VCSELs generally exhibit higher modulation bandwidths: they can be driven at higher current densities and thus reach higher photon densities. However, besides small apertures leading to greater sensitivity for ESD damage, high current density operation is detrimental for reliability (ideally, the operating current density should be kept below  $10 \text{ kA/cm}^2$ ) and large apertures are preferable also from a manufacturing point of view [57]. Additionally, scaling to small aperture diameters can lead to problems from increased scattering losses [83], and increased threshold current density caused by increased lateral current leakage under the oxide aperture [84] and by carriers diffusing laterally

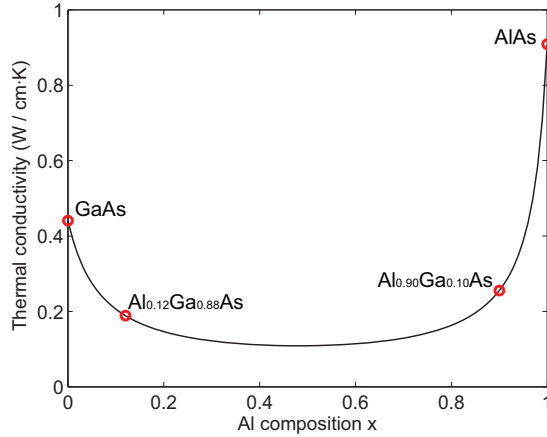


Figure 3.7: Thermal conductivity of  $\text{Al}_x\text{Ga}_{1-x}\text{As}$  as a function of  $x$  [86].

outward from the QWs due to the non-uniform carrier distribution resulting from a small aperture [85].

Intracavity contacts can be beneficial for suppressing heat generation since they can be used to circumvent passing the drive current through the DBRs; the part responsible for most of the electrical resistance in the VCSEL (and thus where most of the resistive heating occurs). This technique is used *e.g.* for the  $n$ -contact in the 980 nm, 35 Gbit/s VCSELs by Chang *et al.* in [17], and for both contacts in combination with a BTJ, ion-implantation, and a dielectric DBR for the 1090 nm 40 Gbit/s VCSELs by Anan *et al.* in [21]. Since doping of the DBRs is not required when using intracavity contacts, this can also help reduce heating from free carrier absorption which is particularly useful at these longer wavelength since  $\alpha_{fc} \propto \lambda^2$  [82]. Heating due to internal absorption can have a significant impact on the thermal rollover. In Paper H we show that when outcoupling through the top mirror ( $\alpha_m^T$ ) is increased, heating from internal absorption is reduced due to a reduction of the internal photon density. In this way, the thermal rollover current was increased by over 40% when increasing the top mirror loss rate from  $0.06 \text{ ps}^{-1}$  to  $0.66 \text{ ps}^{-1}$ , accompanied by a 90% and 160% increase of the slope efficiency and maximum output power, respectively (see Fig. 3.6 (b)).

With rising temperature, carrier leakage starts to increase and deteriorate the performance and reduce internal efficiency. Longer wavelength VCSELs are at an advantage when it comes to preventing carrier leakage since deeper QWs can be used to improve temperature stability. Impressive results with error-free data transmission at 20 and 38 Gbit/s at up to 120 and  $85^\circ\text{C}$ , respectively, have been demonstrated in 980 nm VCSELs using heavily strained InGaAs/AlGaAs QWs in combination with a large detuning [18, 28, 53]. A method of improving carrier confinement applicable also for 850 nm VCSELs is to place an electron blocking layer between the active region and the  $p$ -DBR [87]. However, it is unclear whether in addition to preventing electron overflow to the  $p$ -side, the blocking

layer will increase the hole transport time to the QWs and consequently degrade the high frequency carrier transport properties of the VCSEL. Furthermore, the overall electrical resistance increases when a blocking layer is introduced, leading to increased resistive Joule heating.

Despite efforts for minimizing heat sources, the conversion ratio from electrical to optical power in a VCSEL is typically below 50%. The remaining injected power is converted to heat and efficient heat transport away from the active region to a heat-sink is therefore essential. The standard DBR scheme for 850 nm VCSELs utilizes  $\text{Al}_{0.12}\text{Ga}_{0.88}\text{As}/\text{Al}_{0.90}\text{Ga}_{0.10}\text{As}$  as high/low index material. However, as shown in Fig. 3.7, the thermal conductivity of ternary AlGaAs is significantly lower than for binary GaAs or AlAs. This is due to alloy scattering of phonons [86] and gives longer wavelength VCSELs an advantage when it comes to heat transport because GaAs (and AlAs) is transparent at 980 and 1100 nm, making it possible to use completely binary DBRs at these wavelengths. However, AlAs is transparent also at 850 nm and in the designs presented in Papers A-H, we replace the ternary  $\text{Al}_{0.90}\text{Ga}_{0.10}\text{As}$  with binary AlAs as low index material in the bottom DBR. This improves the effective thermal conductivity of the structure and in Paper B we show a comparatively low thermal impedance of  $1.9^\circ\text{C}/\text{mW}$  for a  $9\ \mu\text{m}$  aperture VCSEL. An indirect but efficient approach to removing heat is to electroplate the VCSEL sidewalls with a metal to form a heat-spreader. Al-Omari *et al.* have managed to increase the maximum output power by 131% along with a considerable improvement of the high speed properties (an increase of the 3dB bandwidth from 6 to 9 GHz) by Cu-plating the sidewalls of the VCSEL to achieve a very low thermal impedance of  $1.0^\circ\text{C}/\text{mW}$  for a  $9\ \mu\text{m}$  aperture 980 nm VCSEL [88]. However, metal-plating introduces an additional parasitic capacitance, which can become detrimental at higher speeds.

### 3.3.4 Electrical parasitics

Electrical parasitics associated with the bondpad and the VCSEL chip itself need to be considered when designing for high speed. Equivalent circuits that fully account for all intrinsic and extrinsic effects taking place in the laser can be used to simulate both electrical and optical characteristics [89]. However, in order to avoid introducing ambiguity in fitting procedures to measured impedance data, it is useful to keep the circuit as simple as possible. Fig 3.8 shows the small signal equivalent circuit commonly used to model the distributed parasitic elements of a VCSEL [24]. As shown in the figure, only a fraction  $i_j$  of the modulation current reaches the intrinsic laser diode represented by  $R_j$ . Consequently, the effects from electrical parasitics can be quantified by a transfer function as [90]

$$H_{par}(f) \equiv \frac{\text{current flowing into the intrinsic diode}}{\text{modulation voltage}} = \frac{i_j(f)}{v_s}. \quad (3.14)$$

In addition to  $R_j$ , the circuit consists of a pad capacitance ( $C_p$ ), a mesa resistance ( $R_m$ ), and a mesa capacitance ( $C_m$ ). The low-pass filter formed by

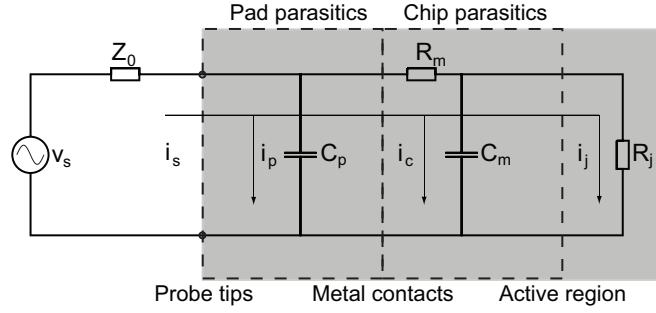


Figure 3.8: Small signal electrical model of VCSEL with driving source. The VCSEL with bondpads is represented by the grayed area.

these distributed parasitic elements limits the effective current modulation of the active region and thereby the modulated light output. To extend the cut-off frequency of this filter as far as possible,  $C_p$ ,  $R_m$ , and  $C_m$  need to be minimized.

The parasitic capacitance associated with the  $p$ - and  $n$ -contact pads ( $C_p$ ) can vary greatly depending on bondpad design and spacing material, but can typically be kept in the order of a few tens of femtofarads by using small area contacts and a thick, low dielectric-constant material (such as benzocyclobutene (BCB) or polyimide) under the signal pad and is thus, if designed correctly, not a limiting factor. In a VCSEL where current is injected through the DBR,  $R_m$  comprises the resistances from the  $p$ - and  $n$ -mirrors, the sheet resistance from the  $n$ -contact layer, and the  $p$ - and  $n$ -contact resistances. As mentioned in Section 2.2.1, much effort has been put into minimizing DBR resistance while keeping optical losses due to free carrier absorption low. This serves the dual purposes of lowering self-heating and, when the VCSEL is modulated, extending the cut-off frequency of the parasitic pole. It should be noted, however, that for the component to be matched to the electrical drive circuitry, the VCSEL impedance should ideally be  $Z_0$  which for electrical measuring equipment usually translates to  $50\ \Omega$ . It is nonetheless desirable to minimize the VCSEL resistance as much as possible in the vicinity of the active region, since heat dissipating from resistive elements close to the junction contribute to performance degradation. If needed, the VCSEL can be electrically matched by increasing the resistance of a part far from the QWs.

For an oxide confined VCSEL,  $C_m$  consists of the junction capacitance ( $C_j$ ) in parallel with the capacitance formed over the insulating oxide layer ( $C_{ox}$ ) serially connected to the capacitance associated with the intrinsic region beneath the oxide aperture ( $C_{int}$ ). For the forward biased VCSEL,  $C_j$  is dominated by the diffusion capacitance over the  $pin$ -junction which is related to the carrier transport properties of the SCH and can be minimized by using a narrow, graded SCH region [77]. Oxide confined VCSELs with a single, thin oxide layer are not well suited for high speed operation since  $C_{ox}$  scales inversely with layer thickness. To reduce the effective area of the aperture contributing to the oxide capacitance, an ion implantation can be used to make the area above the aperture insulating.

Already in 1997, this technique was used successfully to enable a 3dB bandwidth of 21.5 GHz in a small aperture oxide-implanted 850 nm VCSEL [24] and this was the technique used by Johnson *et al.* to first reach 30 Gbit/s with an 850 nm VCSEL [15]. An alternative when using oxide confinement is to employ multiple oxide layers [91, 92]. This approach simplifies fabrication since no additional processing steps are added, and this is the technique used for the Gen I design in Papers A-E, where two oxide layers separated by  $\lambda/2$  are included in the DBR above the active region. In Paper D, impedance measurements and equivalent circuit modeling are used to reveal that despite this effort,  $C_{ox}$  remains the main contributor to the parasitic capacitance and would be beneficial to reduce further. This motivated the updated Gen II VCSEL design presented in Papers F-H, where four additional high Al-content layers are placed above the original two oxide layers in the epitaxial design. Following the technique outlined in [93], these extra layers contain 96% Al which, due to the exponential dependence of oxidation rate on Al content, oxidize at approximately half the rate of the original  $\text{Al}_{0.98}\text{Ga}_{0.02}\text{As}$  layers during the oxidation process. The result is two oxide layers that form the current and optical apertures, and four layers above which help reduce  $C_{ox}$  while having a negligible impact on  $R_m$ .

The equivalent circuit of Fig. 3.8 is useful because each element is related to a physical part of the VCSEL. As is done in Paper D, impedance measurements and equivalent circuit modeling can then be used to extract the individual circuit parameters and their respective dependencies on bias current. For the purpose of relating the impact of parasitics to the small signal modulation response, the equivalent circuit is often replaced by a simple  $RC$ -filter, represented by an additional pole with cut-off frequency  $f_p$ ,

$$H_{par}(f) = \frac{1}{1 + j\frac{f}{f_p}}, \quad (3.15)$$

that is added to the intrinsic transfer function. Combined with the intrinsic modulation response  $H_i(f)$ , the total electrical transfer function then becomes

$$\begin{aligned} H(f) &= |H_i(f) \cdot H_{par}(f)|^2 \\ &= A \cdot \left| \frac{f_r^2}{f_r^2 - f^2 + j\frac{f}{2\pi}\gamma} \cdot \frac{1}{1 + j\frac{f}{f_p}} \right|^2, \end{aligned} \quad (3.16)$$

where  $A$  is an amplitude factor accounting for the slope efficiency of the laser, the dynamic response of the photodetector, and the insertion loss of the microwave probe. Eq. 3.16 is the transfer function that is fitted to measured modulation response to extract the parameters  $f_r$ ,  $\gamma$ , and  $f_p$  and their dependencies on bias current.



## 4 VCSEL fabrication

The first and most critical step towards a functioning VCSEL is the epitaxial growth in which the large set of semiconductor layers of different thicknesses, compositions, and doping levels that make up the VCSEL structure are grown on top of a single crystal wafer. If the epitaxy does not produce a high quality material, all the subsequent fabrication steps are rendered irrelevant. After successful material growth, a series of fabrication steps follow in which optical and electrical confinement and ohmic contacts for current injection are introduced. It is during fabrication that the individual components take form and component design is critical for the final performance of the device as aperture size, chip parasitics, etc. are largely determined by the fabrication process. In the following, a description of the epitaxial material and an outline of the fabrication process and techniques used in this work are presented.

### 4.1 Epitaxial material

Three different epitaxial structures have been used for this work and we label the first two epi-designs Gen I (used in Papers A-E) and the third structure Gen II (used in Papers F-H). All were grown on undoped 3" GaAs substrates by metal-organic vapor phase epitaxy (MOVPE) and supplied by IQE Europe. Although small size samples were used in the device fabrication, the fact that we have employed an industrial supplier of the material demonstrates that the type of epi-structures used have potential for large scale fabrication.

In the first Gen I design, the active region consists of five 4 nm thick strained  $\text{In}_{0.1}\text{Ga}_{0.9}\text{As}$  QWs separated by 6 nm thick  $\text{Al}_{0.37}\text{Ga}_{0.63}\text{As}$  barriers and sandwiched between two undoped, 85 nm thick, linearly graded layers ( $\text{Al}_{0.37}\text{Ga}_{0.63}\text{As} \rightarrow \text{Al}_{0.6}\text{Ga}_{0.4}\text{As}$ ), forming a  $1\lambda$  thick SCH region. The second Gen I structure has an active region comprising three 8 nm thick unstrained GaAs QWs separated by 8 nm  $\text{Al}_{0.3}\text{Ga}_{0.7}\text{As}$  barriers and again sandwiched between two undoped, 85 nm thick, linearly graded layers ( $\text{Al}_{0.3}\text{Ga}_{0.7}\text{As} \rightarrow \text{Al}_{0.6}\text{Ga}_{0.4}\text{As}$ ) in a  $1\lambda$  SCH region. The QW widths were chosen so as to produce a gain peak at the same wavelength in both structures. With increasing In-concentration, the QW thickness needs to be reduced and the Al-content in the barriers increased in order to keep the gain peak at the correct wavelength. To maintain a similar confinement factor in both structures, five QWs were therefore used in the InGaAs active region as opposed to three in the GaAs active region. Both Gen I structures have the

same DBR design, with the top,  $p$ -doped (carbon doped) mirror containing 23 pairs of  $\text{Al}_{0.9}\text{Ga}_{0.1}\text{As}/\text{Al}_{0.12}\text{Ga}_{0.88}\text{As}$  layers. A highly doped ( $\sim 10^{20} \text{ cm}^{-3}$ ) GaAs cap-layer is placed at the very top of the structures to allow for ohmic contact formation. Two 30 nm thick  $\text{Al}_{0.98}\text{Ga}_{0.02}\text{As}$  layers separated by  $\lambda/2$  are included just above the SCH to allow for selective oxidation and the formation of two oxide apertures while keeping current injection uniform and lateral leakage currents low. As discussed in Section 3.3.4, double oxide layers are used to reduce parasitic capacitance. The  $n$ -doped (silicon doped) bottom DBR includes 4 pairs of  $\text{Al}_{0.9}\text{Ga}_{0.1}\text{As}/\text{Al}_{0.12}\text{Ga}_{0.88}\text{As}$  directly below the SCH followed by 28 pairs of  $\text{AlAs}/\text{Al}_{0.12}\text{Ga}_{0.88}\text{As}$  layers and finally an  $n$ -doped GaAs contact layer on the undoped substrate. Modulation doping and compositionally graded interfaces between the DBR layers are used to minimize electrical resistance and free carrier absorption in the final devices. Essentially, the only difference between the two Gen I structures are the active regions: strained InGaAs contra unstrained GaAs QWs and the difference in performance between these two designs are investigated in Papers B and E.

Due to the success of using strained QWs, the Gen II material utilizes the same active region design as the InGaAs-structure from the Gen I VCSELs. The AlAs-containing bottom DBR is identical to the Gen I structure as well. The difference lies in the top DBR, where four 30 nm thick  $\text{Al}_{0.96}\text{Ga}_{0.04}\text{As}$  layers are incorporated above the original two  $\text{Al}_{0.98}\text{Ga}_{0.02}\text{As}$  layers. Due to the strong dependence of oxidation rate on Al-content, these additional layers oxidize at approximately half the rate of the original layers during the wet oxidation process. The end result is reduced parasitic mesa capacitance in the finished Gen II devices.

## 4.2 General processing techniques

The last stage of the VCSEL manufacturing process is the device fabrication. Fabrication techniques including pattern transfer via photolithography, dry etching, chemical vapor deposition (CVD), electron beam evaporation, sputtering, thermal annealing, and wet oxidation are all used when processing oxide confined VCSELs. Additionally, it is important to constantly inspect and control the outcome of every process step during fabrication. For this purpose, microscopy (optical microscopy, scanning electron microscopy (SEM), atomic force microscopy (AFM)) is used to evaluate surfaces and microstructures, profilometers (mechanical and optical) are used for measuring etch depths and film thicknesses, and a parameter analyzer is used for evaluating contact resistances.

### 4.2.1 Lithography

An important part of microprocessing is to be able to transfer small feature size patterns onto the sample. This is done using various lithography techniques.

Standard UV photolithography can be used for feature sizes down to  $\sim 1\mu\text{m}$ , and due to its simplicity, this is the technique used in this work. More advanced photolithography techniques (*e.g.* immersion photolithography using 193 nm ArF excimer lasers) can be used to yield sub 40 nm resolution [94]. If even smaller dimensions are required, it is possible to use electron beam lithography where feature sizes below 10 nm are possible [95] but the improved resolution then comes at the expense of increased cost and reduced throughput.

The standard UV photolithography process starts with spinning a photosensitive resist onto the chip where the viscosity of the resist and the spin speed determine the thickness of the resulting film. After spinning, the sample is exposed to UV radiation through a patterned mask and depending on the type of resist, the exposed (positive resist) or unexposed (negative resist) areas dissolve in the subsequent development and the mask pattern is thus transferred onto the sample. The patterned resist can then be used to protect parts of the surface during etching or deposition of dielectrics or metals.

#### 4.2.2 Thin film deposition

Thin films of both dielectric materials and metals are deposited during the VCSEL fabrication process. Silicon nitride is a dielectric and is used for protection of the chip surface to prevent involuntary oxidation. The silicon nitride can be deposited using various plasma enhanced chemical vapor deposition (PECVD) systems, and in this work, inductively coupled plasma (ICP) PECVD has been the method of choice. The ICP system has an in-situ laser interferometer end-point system that allows for precise thickness control of the deposited films. In the deposition process, silane gas ( $\text{SiH}_4$ ) is injected close to the sample in the process chamber. Here, excited Ar ions from the ICP dissociate the silane which reacts with  $\text{N}_2$  to form silicon nitride on the sample surface. The resulting silicon nitride does not have a precise stoichiometry and is therefore usually denoted  $\text{Si}_x\text{N}_y$ .

In VCSEL processing, patterned thin films of metals are formed in so-called lift-off processes. First, a contact pattern is defined in a spun-on resist through photolithography. Second, the metal is deposited over the entire patterned chip, either by thermal evaporation or by sputtering. Finally, the sample is put in a solvent (usually acetone) where the patterned resist is dissolved, lifting off the metal on top of it in the process (hence the name lift-off). Left is a metal pattern in the areas of the sample where no resist was present during deposition.

In an electron beam evaporation system, an electron beam is generated by *e.g.* thermionic emission and accelerated and directed to a source metal where the kinetic energy of the electrons is converted to thermal energy, thus heating the metal and causing metal atoms to evaporate and form a thin metal film on the sample positioned above. This technique was used to form both the Ni/Ge/Au *n*-contacts and the Ti/Pt/Au *p*-contacts in this work, whereas the Ti/Au bondpad was deposited using a sputter system. In the sputtering process,

an Ar plasma is generated and the ions are accelerated towards a metal source in order to sputter off (hence the name) metal atoms which then deposit on the sample. The sputtering system results in a less directed deposition than thermal evaporation, and therefore gives a better step coverage.

### 4.2.3 Etching

Material removal is done either by wet or dry etching techniques. As the name implies, wet etching utilizes a liquid chemical to remove material (*e.g.* an acid for metals or dielectrics, and an oxidizing agent + an acid for GaAs). This typically leads to a rather isotropic or crystallographically dependent etch and if anisotropic etching with high aspect ratio is required, dry etching techniques, in which an energetic ion beam or a plasma is used to remove material, are preferred.

Inductively coupled plasma reactive ion etching (ICP-RIE) was used for all etch steps in this work. Depending on process parameters (*e.g.* ICP and RF power levels, chamber pressure, gas flow, and gas chemistry), this etch technique can be either mainly chemical or mainly physical as well as highly anisotropic or isotropic. Inert Ar mixed with highly reactive  $\text{SiCl}_4$  or  $\text{Cl}_2$  was used for the AlGaAs mesa etch. During this mainly chemical process, the gas molecules are decomposed into radicals in a plasma and accelerated towards the sample where chemical reactions at the horizontal AlGaAs surfaces form volatile products which desorb and leave the process chamber through the vacuum exhaust. The result is an efficient, highly anisotropic etch process that produces near vertical mesa side-walls. For the  $\text{Si}_x\text{N}_y$  etch steps,  $\text{NF}_3$  (which is highly selective towards AlGaAs) is used in combination with relatively high ICP power and chamber pressure. This results in a more isotropic etch and allows for removal of  $\text{Si}_x\text{N}_y$  on both horizontal and vertical surfaces.

The etch system that was used in this work also provides precise depth control via an in-situ laser interferometer endpoint system. Additionally, the system has two chambers: one for Cl-based etching, and one for F-based etching *and* for PECVD processes. A load-lock system allows for transfers between the chambers without breaking vacuum, a feature that is used for the mesa etch in this work (as described in Section 4.3).

### 4.2.4 Wet oxidation

The oxide aperture is formed in an oxidation furnace where the sample is exposed to a steam atmosphere at temperatures up to  $450^\circ\text{C}$ . Inert nitrogen bubbled through boiling water is used as a carrier gas to transport water steam into the furnace. The furnace chamber and piping are kept at constant temperature and the flow of nitrogen is regulated to achieve a stable and reproducible process. An in-situ monitoring system, consisting of a CCD camera and a microscope with an appropriate illumination wavelength to produce high contrast between

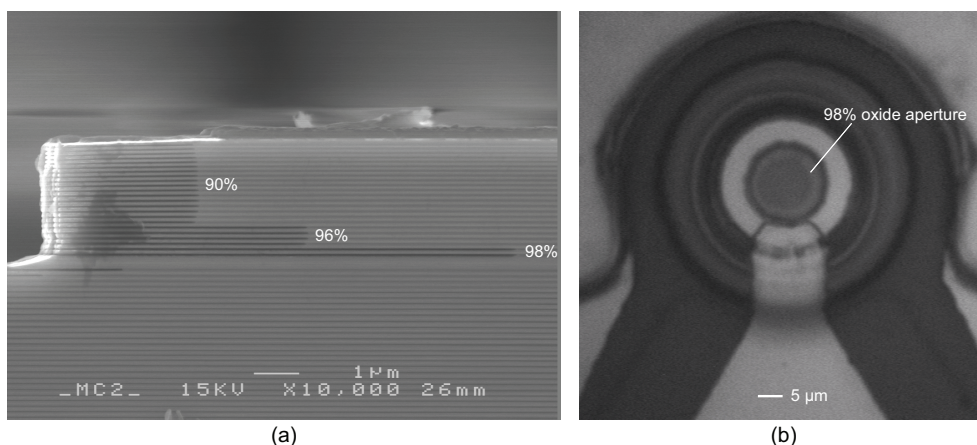


Figure 4.1: (a) SEM micrograph of a cleaved Gen II VCSEL mesa after wet oxidation and (b) IR microscope image of fully fabricated Gen II VCSEL.

oxidized/unoxidized  $\text{Al}_x\text{Ga}_{1-x}\text{As}$  (940 nm illumination was used for this work), is used to control the size of the apertures.

The oxidation rate of  $\text{Al}_x\text{Ga}_{1-x}\text{As}$  is highly dependent on temperature, Al-content, and layer thickness [96, 97]. The strong dependence on Al-content permits for the entire mesa to be exposed to the steam environment since the oxidation rate of layers other than the ones with 96 or 98% Al-content is small. The temperature of the furnace is calibrated to give a manageable oxidation rate and circular apertures. 420°C was used for the VCSELs in this work, resulting in an oxidation rate of  $\sim 0.26$  and  $\sim 0.15$   $\mu\text{m}/\text{min}$  for the  $\text{Al}_{0.98}\text{Ga}_{0.02}\text{As}$  and  $\text{Al}_{0.96}\text{Ga}_{0.04}\text{As}$  layers, respectively. Fig. 4.1 (a) shows a SEM micrograph of a cleaved Gen II VCSEL mesa and (b) an IR microscope image of a fully processed VCSEL, illustrating the contrast difference between oxidized/unoxidized AlGaAs attainable with the monitoring system.

### 4.3 Fabrication process for high speed VCSELs

The device fabrication in this work follows standard fabrication techniques for oxide confined VCSELs. The process used for the Gen II VCSEL fabrication is summarized below and in Fig. 4.2 (a)-(i).

Before fabrication starts, the 3" wafer is cleaved into smaller chips measuring  $8 \times 10$  mm. After cleaning, Ti/Pt/Au alignment marks and top  $p$ -contact rings are deposited by electron beam evaporation, see Fig. 4.2 (a). Before the mesas are defined, a thin layer of  $\text{Si}_x\text{N}_y$  (160 nm) is deposited over the entire chip to protect the unetched surfaces during the oxidation process. The circular mesa structures are then defined through photolithography and the ICP-RIE system is used to remove the  $\text{Si}_x\text{N}_y$  not protected by resist in a  $\text{NF}_3$  plasma after which the mesas are etched using Ar/ $\text{SiCl}_4$  and Ar/ $\text{Cl}_2$  chemistry (Fig. 4.2 (b)). Four different mesa diameters are used (28, 30, 32, and 34  $\mu\text{m}$ ) to give a variation

over the chip in the final oxide aperture diameters. The target etch depth is 3.2-3.4  $\mu\text{m}$  and the laser interferometer system is used for depth control. It is critical not to etch too far into the bottom mirror, as etching into the binary AlAs layers (which start at 3.8  $\mu\text{m}$ ) would cause serious problems during oxidation. Without breaking vacuum after the etch, a 160 nm thick protective layer of  $\text{Si}_x\text{N}_y$  is then deposited on the chip (using the PECVD function of the system) to protect the surface of the etched sample from the atmosphere and during oxidation. If the chip surface is not protected and a moderately high Al-content layer happens to be exposed, exposure to air oxidizes the surface within minutes and makes the later deep etch to the contact layer difficult with a resulting rough, uneven chip surface. A photolithography step and subsequent selective  $\text{NF}_3$  etching of the  $\text{Si}_x\text{N}_y$  on the mesa sidewalls serving to expose the 96 and 98% Al-content layers follows before the chip is oxidized at 420°C. The progress of the oxide front is monitored in-situ with the IR illuminated microscope and the process is stopped after approximately 40 min, resulting in aperture sizes in the range 7-13  $\mu\text{m}$  depending on mesa diameter (Fig. 4.2 (c)). Following a photolithography step to define 50  $\mu\text{m}$  diameter mesas, removal of the protective  $\text{Si}_x\text{N}_y$  and a deep etch down to the  $n$ -contact layer (using the same ICP-RIE system and recipe as for the mesa etch), yet another photolithography step allows for electron beam evaporation of the Ni/Ge/Au  $n$ -contacts, see Figs. 4.2 (d) and (e). Germanium is included in the composition because the  $n$ -contact layer is not sufficiently doped to allow for ohmic contacting without additional doping. In the subsequent rapid thermal annealing, Ge alloys with the contact layer, thereby heavily doping it and generating ohmic contacts. To minimize pad capacitance, the doped contact layer is then removed in the areas underneath where the top bondpad will be positioned, again using the ICP system after a photolithography step (see Fig. 4.2 (f)). Photosensitive Benzocyclobutene (BCB) 4026-46 is used to planarize the  $\sim 7.5$   $\mu\text{m}$  high mesa structures (Fig. 4.2 (g)), and in the final process step, Ti/Au bondpads are defined through photolithography and sputtered in place to allow for probing and evaluation of the components (Fig. 4.2 (h)). After initial tests, a shallow surface etch of the top DBR (or an  $\text{Si}_x\text{N}_y$  or  $\alpha$ -Si AR-coat) is made using the ICP-RIE system using Ar/ $\text{SiCl}_4$  chemistry and low RF power (and zero ICP power) to achieve a slow, stable etch-rate and reach the optimum reflectivity and photon lifetime in the finished VCSELs, see Fig. 4.2 (i).

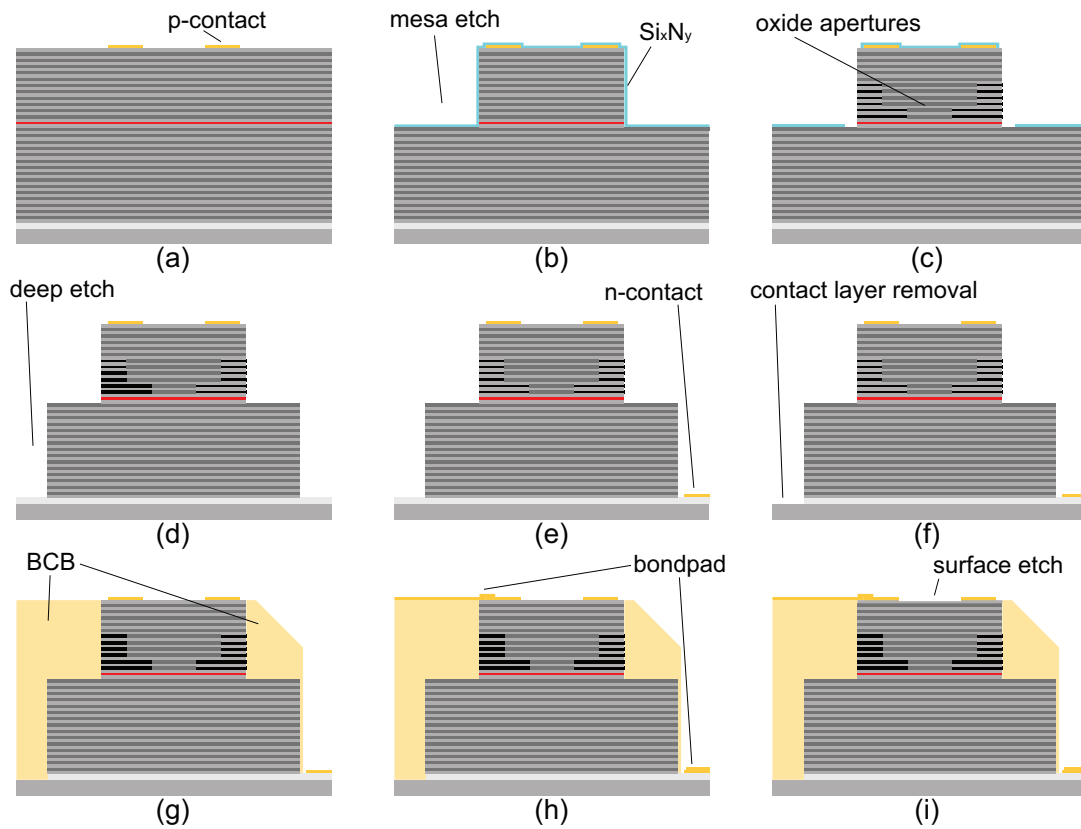


Figure 4.2: Schematic illustration of the major process steps for the Gen II high speed 850 nm VCSEL fabrication: (a) top contact deposition, (b) mesa etch and Si<sub>x</sub>N<sub>y</sub> deposition, (c) Si<sub>x</sub>N<sub>y</sub> opening and oxidation, (d) deep etch, (e) n-contact deposition, (f) contact layer removal, (g) BCB processing, (h) bondpad sputtering, (i) shallow etch or AR-coat.



# 5 High speed measurements

A range of high speed measurements are necessary to evaluate the dynamic performance of the fabricated VCSELs. When performing these measurements it is important to appreciate that the acquired results reflect the dynamic performance of the entire measurement setup, including electrical probes, VCSEL, coupling optics, fiber, detector, amplifiers, and cabling. To get a result mirroring the true VCSEL performance, careful calibration and control of all additional measurement components is therefore essential. A sufficiently fast photodetector is of particular importance but unfortunately, the availability of 850 nm multimode detectors with sufficient bandwidth to allow for measurements at bit-rates  $>30$  Gbit/s is almost non-existent. This is not due to an intrinsic limit in possible detector performance, but rather that there previously have not been any multimode 850 nm components capable of transmitting at these high bit-rates and consequently no market for the corresponding detectors. However, there is an increasing demand and some new detectors are emerging on the market, for example, VI Systems have recently developed a 30 GHz multimode detector designed for 850 nm. In this work, we use a New Focus 1481-S-50 25 GHz fiber coupled multimode detector for all modulation response measurements, the eye-diagram recordings from Paper A, B and C, and the bit-error measurements in Paper C. For the 40 Gbit/s experiments in Paper H, we use the VI Systems detector model D30-850M.

## 5.1 Small signal modulation response

A good first indicator of high speed performance is to measure the small signal frequency response ( $S_{21}$ ) of the VCSEL using a network analyzer. From this measurement,  $f_{3dB}$ ,  $f_r$ ,  $\gamma$ , and  $f_p$  and their respective dependencies on bias current can be extracted through curve-fitting Eq. 3.16 to the measured data and conclusions can be made as to which parameters are limiting the dynamic performance. It is in principle possible to attain both phase and magnitude of the modulation response if the system is calibrated accordingly. However, only magnitude information of the detector frequency response is typically available in the product calibration sheet and even though phase response information in principle can be extracted from this data [98], we measure only the magnitude of the frequency response ( $|S_{21}|$ ) as it requires less calibration and still provides much information ( $|S_{21}(f)| = H(f)$  from Eq. 3.16).

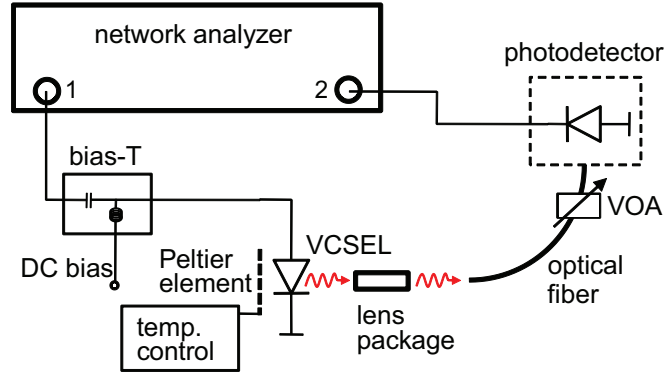


Figure 5.1: Experimental setup for measuring the small signal modulation response ( $|S_{21}|$ ). The same measurement setup is used for the impedance ( $S_{11}$ ) measurements.

Fig. 5.1 shows a schematic of the setup used for measuring the modulation response. The bias current is combined with the sinusoidal small signal modulation signal from port 1 of the network analyzer through a high frequency bias-T and fed to the VCSEL by a high speed RF probe (Picoprobe 40A-GSG-100-P from GGB Industries). The design of the VCSEL bondpad is such that it is matched with the  $100\ \mu\text{m}$  pitch of the ground-signal-ground configured probe. A Peltier element and a thermistor are attached to the VCSEL submount to enable measurements at elevated temperatures. The modulated light is coupled to a short (1 m long)  $50\ \mu\text{m}$  multimode fiber via an AR coated lens system that matches the numerical aperture of the VCSEL with that of the fiber. This coupling system results in  $>60\%$  coupling efficiency and minimizes optical feedback to the laser. The fiber is connected to the photodetector which in turn is connected to port 2 of the network analyzer. If the fiber-coupled output power is high, a variable optical attenuator (VOA) is included to keep the the photodetector from saturating. A thru calibration is made to remove any influence from attenuation in the cables and the bias-T prior to the measurement. Before curve-fitting, the data acquired from the measurements is compensated for the magnitude response of the detector and the insertion loss of the RF probe (with data obtained from the calibration sheets provided with the respective equipment). The tool used for the  $|S_{21}|$  measurement is an Anritsu 37397C (40 MHz - 65 GHz) network analyzer.

## 5.2 Electrical impedance

Impedance measurements are useful for de-embedding the various parasitic elements contained within the VCSEL and determine to what extent each element contribute to the total electrical parasitics. The measurement is equivalent to a measurement of  $S_{11}$  via

$$Z_L = Z_0 \frac{1 + S_{11}}{1 - S_{11}}, \quad (5.1)$$

where  $Z_L$  is the VCSEL impedance and  $Z_0$  is the characteristic impedance of the measuring equipment (usually  $50 \Omega$ ).

The same experimental setup is used as for the  $S_{21}$  measurements but since this is a reflection measurement, only port 1 of the network analyzer is needed. Since capacitive elements are incorporated in the VCSEL structure (see Fig. 3.8),  $S_{11}$  is complex-valued and information from both magnitude and phase is required for an accurate measurement. A full calibration up to the probe tips is therefore essential and for this purpose, a calibration substrate CS-5 from GGB Industries together with the appropriate calibration kit loaded into the network analyzer is used together with an  $S_{11}$  1-port calibration. This calibration uses the short, open, and load pattern on the calibration substrate and is the most accurate calibration for  $S_{11}$  measurements. The calibration is performed just before the experiment to avoid system drift. The tool used for the  $S_{11}$  measurement is an Agilent N5230A PNA-L (10 MHz-20 GHz) network analyzer.

### 5.3 Transmission experiments

In real data transmission applications, the modulation amplitude is significantly larger than what is used in the small signal experiments described above. Typically, the VCSEL is modulated by abruptly changing the current from a low off-state (representing a 0) to a high on-state (representing a 1). Nonetheless, small signal analysis gives approximate information about the laser behavior during large signal modulation and as a rule of thumb, the maximum large signal bit-rate is approximately  $1.3 \cdot f_{3dB}$  when a non-return-to-zero (NRZ) binary modulation format is used [99], *i.e.* when the 3dB bandwidth is 10 GHz, error-free transmission at 13 Gbit/s is possible.

More direct information about a laser's performance during large signal modulation can be obtained by studying eye diagrams and measuring bit-error-rates (BER), as is done in Papers C and G where error-free transmission (defined here as  $BER < 10^{-12}$ ) up to 32 and 40 Gbit/s is demonstrated, respectively. Eye diagrams are used to examine the shape of the optical waveform generated by modulating the VCSEL with a binary data signal. Path A in Fig. 5.2 is used for this measurement. A non return to zero pseudorandom bit sequence (NRZ-PRBS) is generated by a pattern generator, combined with the drive current in the bias-T, and fed to the VCSEL through the same high speed RF probe as used for the  $S$ -parameter measurements. The modulated light output is butt coupled to a short  $62.5 \mu\text{m}$  multimode fiber which in turn is coupled either directly to the photodetector, or via different lengths of OM3 fiber to see the fiber influence on eye quality. OM3 fiber has a bandwidth-distance product limited to  $2 \text{ GHz}\cdot\text{km}$  by modal dispersion, and thus some signal quality degradation is

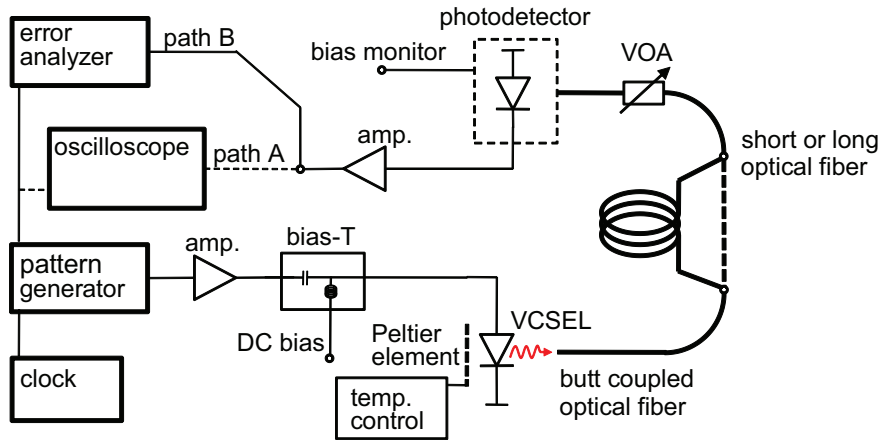


Figure 5.2: Experimental setup for recording eye diagrams (path A) and measuring BER (path B).

expected when propagating a high bit-rate signal over long distances<sup>1</sup>. To be able to conduct measurements as a function of received optical power, a variable optical attenuator (VOA) is included in the measurement setup just before the photodetector. The optical power is monitored through a DC bias-monitor built into the photodetector. The electrical signal from the detector is amplified and connected to a high speed oscilloscope synchronized with the pattern generator. The oscilloscope displays an overlay of the received data pattern, forming the characteristic eye diagrams and allowing for fundamental qualities such as rise and fall times, overshoot/undershoot and timing jitter to be statistically analyzed for many different combinations of ones and zeros. A pseudorandom data pattern is used to reflect that real communication signals are not repetitive and to highlight pattern-dependent problems, such as slow rise time or excessive overshoot, which would be overlooked if studying *e.g.* a single pulse waveform.

Eye diagrams serve mainly as a tool for optimizing drive conditions and equipment to yield a clear data signal producing as few errors as possible when detected. The fundamental measure of performance for a digital communication system is how accurately the receiver can determine the logic state of each transmitted bit. This is quantified by the BER which is defined as the probability of incorrect identification of a bit by the decision circuit in the receiver. BER is a statistical parameter and the accuracy of the measured value depends on the gating time over which the data is collected. For high error rates ( $\text{BER} \geq 10^{-9}$ ), the BER reaches a stable value relatively fast at high bit-rates and can be accurately determined. To measure very low BER, however, a longer gating time is necessary. Assuming all errors due to nonrandom events such as external interference have been eliminated, the required gating time ( $t$ ) at which no errors can occur for an upper bound ( $p$ ) on the BER can be calculated as [100]

<sup>1</sup>Higher speed fiber, such as OM4 with a bandwidth-distance product of 4.7 GHz·km, would allow for longer propagation before signal degradation.

$$t = -\frac{\ln(1 - c)}{p \cdot B}, \quad (5.2)$$

where  $B$  is the bit-rate and  $c$  the statistical confidence level. To be able to claim a BER less than  $10^{-13}$  with 95% confidence at a bit-rate of 25 Gbit/s then translates into a required gating time of 20 minutes with no detected errors. It is therefore essential to optimize the experimental setup and the signal before starting the measurements. This is commonly done by optimizing the corresponding eye diagram.

Path B in Fig. 5.2 is used for BER measurements. Together with the pattern generator, the error analyzer makes up a so-called bit error rate tester (BERT). The pattern generator creates the test pattern of a predetermined word length ( $2^7 - 1$  was used for this work) from an external (or internal) clock signal at the selected data rate. This pattern is then injected into the system under test and received at the error analyzer's data input. The error analyzer includes an internal pattern generator that produces an exact replica of the test pattern and a comparator circuit that checks every received bit against it. An error is logged each time a received bit differs from the internally generated pattern. To ensure that the error analyzer and pattern generator operate at identical bit-rates, the clock output from the pattern generator is directly connected to the error analyzer's clock input<sup>2</sup>. The error analyzer includes a system for automatically synchronizing its internally generated pattern to the incoming data and for optimizing the decision levels of the comparator circuit to produce as few errors as possible. The BERT system used in the experiments of Papers C and G consists of an SHF 12100B Bit Pattern Generator and an SHF 11100B Error Analyzer which are capable of tests at bit-rates up to 56 Gbit/s. In actual applications, uncooled operation of the VCSEL is preferred to keep power consumption and module cost at a minimum. In datacom, for example, uncooled operation at 85°C and above is required. Therefore, it is important to evaluate the link performance at elevated temperatures and a Peltier element coupled with a thermistor is included in the VCSEL submount to allow for precise control of the ambient temperature.

---

<sup>2</sup>In real applications, *i.e.* when the signal source and the detector are not in close physical proximity, the clock signal is included in the transmitted data and the detector's clock signal must be recovered directly from the data.



## 6 Summary of papers

This thesis consists of eight appended papers focused on the dynamic properties of high speed 850 nm VCSELs. Papers A and C experimentally demonstrate the high speed capabilities of VCSELs with strained QWs. In Paper B, a detailed experimental comparison between using unstrained and strained QWs in VCSELs is conducted. Paper D employs numerical calculations to confirm the advantages of using strained QWs, supporting the results from Paper B. In Paper E, the high speed limitation from parasitic elements in the Gen I VCSEL structure is investigated, ultimately leading to the updated Gen II design presented in Papers F-H. The importance of optimized photon lifetime is illustrated in Papers F and G, where record high modulation bandwidths and error-free data transmission rates are demonstrated, respectively. Paper H presents a detailed analysis of the high speed performance of the Gen II VCSELs with a focus on the influence of the photon lifetime.

### Paper A

**”Large aperture 850 nm VCSELs operating at bit rates up to 25 Gbit/s,”** *Electron. Lett.*, vol. 44, no. 15, pp. 907-908, July 2008.

A 3dB bandwidth exceeding 20 GHz is measured for a 9  $\mu\text{m}$  aperture VCSEL operating at 850 nm. Open eye diagrams are demonstrated at room temperature at 20 and 25 Gbit/s at a bias current density of 10 kA/cm<sup>2</sup>. The VCSEL design is optimized for high speed performance with a double oxide aperture, binary bottom DBR, and strained InGaAs QWs.

**My contribution:** I participated in the design work and fabricated the VCSELs. I performed all the measurements, the analysis of the results, and wrote the paper. I also presented the results at the International Semiconductor Laser Conference 2008 (Sorrento, Italy).

### Paper B

**”High-speed, low-current-density 850 nm VCSELs,”** *IEEE J. Sel. Topics Quantum Electron.*, vol. 15, no. 3, pp. 694-703, May/June 2009 (invited paper).

In this paper we report on the design, fabrication and evaluation of large aperture oxide confined 850 nm VCSELs optimized for high speed operation. A comparative study of the performance of two similar designs leads to the conclusion that an active region composed of strained InGaAs QWs results in superior high speed performance compared to traditional GaAs QWs due to higher differential gain. A maximum 3dB bandwidth of 20 GHz is demonstrated at room temperature for the InGaAs VCSEL compared to 16.5 GHz for the GaAs VCSEL. Curve fits of the small signal transfer function to the measured modulation response reveal that the high speed performance of both VCSELs is limited mainly by parasitics and that design efforts therefore should be put into extending the parasitic cut-off frequency. Open eye diagrams are demonstrated at 30 Gbit/s up to 55°C and at 25 Gbit/s up to 85°C at a bias current density of 11 kA/cm<sup>2</sup> for the InGaAs VCSEL.

**My contribution:** I participated in the design work and fabricated the VCSELs, performed all measurements and did the analysis of the results. I wrote the paper and presented the results at the International Nano-Optoelectronics Workshop 2009 (Berlin, Germany).

## Paper C

**”32 Gbit/s multimode fibre transmission using high-speed, low current density 850 nm VCSEL,”** *Electron. Lett.*, vol. 45, no. 7, pp. 366-368, March 2009.

Error-free transmission at 32 Gbit/s is demonstrated over 50 m of OM3 fiber with a large aperture InGaAs VCSEL at room temperature and 11 kA/cm<sup>2</sup> bias current density. At the time of publication, this was the highest bit-rate at which error-free transmission had been reported for 850 nm VCSELs. Successful 25 Gbit/s transmission over 100 m of OM3 fiber is demonstrated up to 85°C at 14 kA/cm<sup>2</sup>.

**My contribution:** I participated in the design work and fabricated the VCSELs, performed all measurements together with F. Hopfer at TU Berlin and did the analysis of the results. I wrote the paper and presented the results at the International Nano-Optoelectronics Workshop 2009 (Berlin, Germany) and at the Conference on Lasers and Electro-Optics 2009 (Baltimore, USA).

## Paper D

**”Impedance characteristics and parasitic speed limitations of high-speed 850-nm VCSELs,”** *IEEE Photon. Technol. Lett.*, vol. 21, no. 24, pp. 1840-1842, December 2009.

This paper presents results from impedance measurements and equivalent circuit

modeling of the VCSELs from Papers A-C. The results confirm the findings from Paper B that device parasitics have a major impact on the modulation speed. To alleviate the impact from parasitics, an additional few oxide layers is proposed to be included in an updated VCSEL structure for a further reduction of mesa capacitance. It is predicted that this design modification may allow for a modulation bandwidth sufficient for error-free transmission at 40 Gbit/s.

**My contribution:** I fabricated the VCSELs and aided Y. Ou in the impedance measurements and equivalent circuit modelling. I co-authored the paper and was the corresponding author.

## Paper E

**”Active region design for high-speed 850-nm VCSELs,”** *IEEE J. Quantum Electron.*, vol. 46, no. 4, pp. 506-512, April 2010.

This paper presents results from gain calculations for strained InGaAs/AlGaAs QWs with the gain peak at 850 nm with the purpose of optimizing the design with respect to differential gain and threshold carrier density. A design enabling a doubling of the differential gain (compared to unstrained GaAs/AlGaAs QWs) is presented, confirming the conclusions from Paper B that the superior high speed performance from using strained InGaAs QWs is due to a higher differential gain. Values for the differential gain are extracted from modulation response measurements and transfer function fits, resulting in a good agreement between the calculated and the experimentally derived values for both strained and unstrained QWs.

**My contribution:** I fabricated the VCSELs and performed the temperature dependent measurements and the analysis of the measurement results. I co-authored the paper and was the corresponding author.

## Paper F

**”Speed enhancement of VCSELs by photon lifetime reduction,”** *Electron. Lett.*, vol. 46, no. 13, pp. 938-940, June 2010.

In this paper, it is demonstrated that a significant increase of the modulation bandwidth can be achieved by reducing the photon lifetime through an associated decrease of the damping of the intrinsic modulation response. An updated VCSEL design (Gen II) based on the findings from Paper D is presented, with four additional oxide layers included in the top DBR for reduced capacitance. A record high modulation bandwidth of 23 GHz is demonstrated for a 7  $\mu\text{m}$  VCSEL with a photon lifetime optimized through a  $\sim 40$  nm shallow surface etch of the top DBR.

**My contribution:** I proposed the parametric investigation of the effects of reduced top DBR reflectivity (reduced photon lifetime). I participated in the design work and fabricated the VCSELs. I performed all the measurements and the analysis of the results. I wrote the paper and presented the results at the International Semiconductor Laser Conference 2010 (Kyoto, Japan).

## Paper G

**"40 Gbit/s error-free operation of oxide-confined 850 nm VCSEL,"** *Electron. Lett.*, vol. 46, no. 14, pp. 1014-1016, July 2010.

Error-free transmission at 40 Gbit/s over a short length of multimode fiber, and at 35 Gbit/s over 100m multimode fiber, using the VCSEL from Paper F is demonstrated. This is the highest transmission speed ever demonstrated with an 850 nm VCSEL.

**My contribution:** I fabricated the VCSELs, performed all the measurements together with A. Nadochiy at TU Berlin, and did the analysis of the results. I wrote the paper and presented the results at the International Semiconductor Laser Conference 2010 (Kyoto, Japan).

## Paper H

**"Impact of photon lifetime on high speed VCSEL performance,"** *IEEE J. Sel. Topics Quantum Electron.*, accepted for publication 2011 (invited paper).

This invited paper presents a detailed analysis of the static and dynamic characteristics of the Gen II VCSELs from Papers F-G. In particular, the impact of reduced photon lifetime (through a shallow (0-55 nm) surface etch applied to the top DBR after device fabrication) on all basic static and dynamic laser parameters is studied. From transfer function fits it is found that, due to a trade-off between resonance frequency and damping, there is an optimum photon lifetime for maximum modulation bandwidth.

**My contribution:** I participated in the design work and fabricated the VCSELs. I performed all the measurements and the analysis of the results. I wrote the paper and presented parts of the results at the International Semiconductor Laser Conference 2010 (Kyoto, Japan) and at Photonics West 2011 (San Francisco, USA).

# References

- [1] I. Hayashi, M. Panish, P. Foy, and S. Sumski, “Junction lasers which operate continuously at room temperature,” *Appl. Phys. Lett.*, vol. 17, no. 3, pp. 109–11, Aug. 1970.
- [2] K. Kao and G. Hockham, “Dielectric-fibre surface waveguides for optical frequencies,” *Proc. IEE*, vol. 113, no. 7, pp. 1151–1158, 1966.
- [3] F. Kapron, D. Keck, and R. Maurer, “Radiation losses in glass optical waveguides,” *Appl. Phys. Lett.*, pp. 423–5, Nov. 1970.
- [4] R. Mears, L. Reekie, I. Jauncey, and D. Payne, “Low-noise erbium-doped fibre amplifier operating at  $1.54\ \mu\text{m}$ ,” *Electron. Lett.*, vol. 23, no. 19, pp. 1026–8, 10 Sept. 1987.
- [5] H. Soda, K. Iga, C. Kitahara, and Y. Suematsu, “GaInAsP/InP surface emitting injection lasers,” *Jpn. J. Appl. Phys.*, vol. 18, no. 12, pp. 2329–30, Dec. 1979.
- [6] J. Tatum, “VCSEL proliferation,” in *Proc. SPIE*, vol. 6484, no. 1, Feb. 2007, pp. 648 403–1–7.
- [7] N. Ledentsov, “Deliverable 5.1 of the European project VISIT,” Tech. Rep. [Online]. Available: [http://www.visit.tu-berlin.de/v-menu/public\\_deliverables/](http://www.visit.tu-berlin.de/v-menu/public_deliverables/)
- [8] K. Hahn, M. Tan, Y. Houng, and S. Wang, “Large area multitransverse-mode VCSELs for modal noise reduction in multimode fibre systems,” *Electron. Lett.*, vol. 29, no. 16, pp. 1482–1483, 1993.
- [9] [Online]. Available: [http://www.infinibandta.org/content/pages.php?pg=technology\\_overview](http://www.infinibandta.org/content/pages.php?pg=technology_overview)
- [10] [Online]. Available: <http://www.fibrechannel.org/roadmaps>
- [11] J. Koomey, “Worldwide electricity used in data centers,” *Environ. Res. Lett.*, vol. 3, no. 3, pp. 034 008 1–8, 2008.
- [12] C. Schow, F. Doany, and J. Kash, “Get on the optical bus,” *IEEE Spectrum*, vol. 47, no. 9, pp. 32–56, 2010.

- [13] C. Xie, N. Li, C. Lei, X. Sun, W. Luo, L. Zhao, C. Helms, C. Liu, D. Jessen, and R. Carson, “New high speed VCSEL product development at Emcore,” in *Proc. SPIE*, vol. 7952, no. 1, Feb. 2011, pp. 795 206–1–11.
- [14] D. Gazula, J. Guenter, R. Johnson, G. Landry, A. MacInnes, G. Park, J. Wade, J. Biard, and J. Tatum, “Emerging VCSEL technologies at Finisar,” in *Proc. SPIE*, vol. 7615, 2010, pp. 761 506–1–8.
- [15] R. Johnson and D. Kuchta, “30 Gb/s directly modulated 850 nm datacom VCSELs,” in *Proc. Conference on Lasers and Electro-Optics*, 2008, paper CPDB2.
- [16] S. Blokhin, J. Lott, A. Mutig, G. Fiol, N. Ledentsov, M. Maximov, A. Nadochiy, V. Shchukin, and D. Bimberg, “Oxide-confined 850 nm VCSELs operating at bit rates up to 40 Gbit/s,” *Electron. Lett.*, vol. 45, no. 10, pp. 501–503, 2009.
- [17] Y.-C. Chang, C. Wang, and L. Coldren, “High-efficiency, high-speed VCSELs with 35 Gbit/s error-free operation,” *Electron. Lett.*, vol. 43, no. 19, pp. 1022–1023, 2007.
- [18] W. Hofmann, P. Moser, P. Wolf, A. Mutig, M. Kroh, and D. Bimberg, “44 Gb/s VCSEL for optical interconnects,” in *Proc. Optical Fiber Communication Conference*, 2011, paper PDPC5.
- [19] N. Suzuki, H. Hatakeyama, K. Fukatsu, T. Anan, K. Yashiki, and M. Tsuji, “25-Gbps operation of 1.1- $\mu$ m-range InGaAs VCSELs for high-speed optical interconnections,” in *Proc. Optical Fiber Communication Conference*, 2006, paper OFA4.
- [20] K. Fukatsu, K. Shiba, Y. Suzuki, N. Suzuki, H. Hatakeyama, T. Anan, K. Yashiki, and M. Tsuji, “30-Gbps transmission over 100 M-MMFs (GI32) using 1.1  $\mu$ m-range VCSELs and receivers,” in *Proc. IEEE 19th International Conference on Indium Phosphide and Related Materials*, 2007, pp. 434–437, paper WeB3-4.
- [21] T. Anan, N. Suzuki, K. Yashiki, K. Fukatsu, H. Hatakeyama, T. Akagawa, K. Tokutome, and M. Tsuji, “High-speed InGaAs VCSELs for optical interconnections,” in *Proc. International Symposium on VCSELs and Integrated Photonics*, Dec. 2007, paper E-3.
- [22] R. Dangel, C. Berger, R. Beyeler, L. Dellmann, M. Gmur, R. Hamelin, F. Horst, T. Lamprecht, T. Morf, S. Oggioni, M. Spreafico, and B. Offrein, “Polymer-waveguide-based board-level optical interconnect technology for datacom applications,” *IEEE Trans. Adv. Packag.*, vol. 31, no. 4, pp. 759–767, 2008.

- [23] D. Kuchta, P. Pepeljugoski, and Y. Kwark, "VCSEL modulation at 20 Gb/s over 200 m of multimode fiber using a 3.3 V SiGe laser driver IC," in *Digest of the IEEE/LEOS Summer Topical Meetings*, 2001, pp. 49–50.
- [24] K. Lear, V. Hietala, H. Hou, J. Banas, B. Hammons, J. Zolper, and S. Kilcoyne, "Small and large signal modulation of 850 nm oxide-confined vertical-cavity surface-emitting lasers," in *Proc. Conference on Lasers and Electro-Optics*, V. Hietala, Ed., vol. 11, 1997, pp. 193–194, paper CWA2.
- [25] C. Schow, F. Doany, C. Baks, Y. Kwark, D. Kuchta, and J. Kash, "A single-chip CMOS-based parallel optical transceiver capable of 240-Gb/s bidirectional data rates," *J. Lightw. Technol.*, vol. 27, no. 7, pp. 915–929, 2009.
- [26] J. Kash, F. Doany, D. Kuchta, P. Pepeljugoski, L. Schares, J. Schaub, C. Schow, J. Trehwella, C. Baks, Y. Kwark, C. Schuster, L. Shan, C. Patel, C. Tsang, J. Rosner, F. Libsch, R. Budd, P. Chiniwalla, D. Guckenberger, D. Kucharski, R. Dangel, B. Offrein, M. Tan, G. Trott, D. Lin, A. Tandon, and M. Nystrom, "Terabus: a chip-to-chip parallel optical interconnect," in *Proc. IEEE/LEOS 18th Annual Meeting*, 2005, pp. 363–364.
- [27] L. Schares, J. Kash, F. Doany, C. Schow, C. Schuster, D. Kuchta, P. Pepeljugoski, J. Trehwella, C. Baks, R. John, L. Shan, Y. Kwark, R. Budd, P. Chiniwalla, F. Libsch, J. Rosner, C. Tsang, C. Patel, J. Schaub, R. Dangel, F. Horst, B. Offrein, D. Kucharski, D. Guckenberger, S. Hegde, H. Nyikal, C.-K. Lin, A. Tandon, G. Trott, M. Nystrom, D. Bour, M. Tan, and D. Dolfi, "Terabus: terabit/second-class card-level optical interconnect technologies," *IEEE J. Sel. Topics Quantum Electron.*, vol. 12, no. 5, pp. 1032–1044, 2006.
- [28] A. Mutig, G. Fiol, P. Moser, D. Arsenijevic, V. Shchukin, N. Ledentsov, S. Mikhlin, I. Krestnikov, D. Livshits, A. Kovsh, F. Hopfer, and D. Bimberg, "120°C 20 Gbit/s operation of 980 nm VCSEL," *Electron. Lett.*, vol. 44, no. 22, pp. 1305–6, Oct. 2008.
- [29] A. Mutig, J. Lott, S. Blokhin, P. Wolf, P. Moser, W. Hofmann, A. Nadtochiy, A. Payusov, and D. Bimberg, "Highly temperature-stable modulation characteristics of multioxide-aperture high-speed 980 nm vertical cavity surface emitting lasers," *Appl. Phys. Lett.*, vol. 97, no. 15, pp. 151101–1–3, 2010.
- [30] N. Tsukiji, S. Imai, K. Takaki, H. Shimizu, Y. Kawakita, T. Takagi, K. Hiraiwa, J. Yoshida, H. Shimizu, and A. Kasukawa, "Low power consumption and highly reliable 1060 nm vcsels for parallel optical interconnection," in *Proc. IEEE Photonics Society 23rd Annual Meeting*, 2010, pp. 242–243.

- [31] K. Takaki, S. Imai, S. Kamiya, H. Shimizu, Y. Kawakita, K. Hiraiwa, T. Takagi, H. Shimizu, J. Yoshida, T. Ishikawa, N. Tsukiji, and A. Kasukawa, “1060nm VCSEL for inter-chip optical interconnection,” in *Proc. SPIE*, vol. 7952, no. 1, Feb. 2011, pp. 795 204–1–7.
- [32] D. Miller, “Device requirements for optical interconnects to silicon chips,” *Proc. IEEE*, vol. 97, no. 7, pp. 1166–1185, 2009.
- [33] T. Maiman, “Stimulated optical radiation in ruby,” *Nature*, vol. 187, no. 4736, pp. 493–494, 1960.
- [34] “NIF Fun Facts,” National Ignition Facility, Tech. Rep. [Online]. Available: [https://lasers.llnl.gov/multimedia/publications/pdfs/pk\\_fun\\_facts.pdf](https://lasers.llnl.gov/multimedia/publications/pdfs/pk_fun_facts.pdf)
- [35] D. Bergman and M. Stockman, “Surface plasmon amplification by stimulated emission of radiation: quantum generation of coherent surface plasmons in nanosystems,” *Phys. Rev. Lett.*, vol. 90, no. 2, pp. 027 402–1–4, 2003.
- [36] M. A. Noginov, G. Zhu, A. M. Belgrave, R. Bakker, V. M. Shalaev, E. E. Narimanov, S. Stout, E. Herz, T. Suteewong, and U. Wiesner, “Demonstration of a spaser-based nanolaser,” *Nature*, vol. 460, no. 7259, pp. 1110–1112, Aug. 2009.
- [37] C. Schow, F. Doany, A. Rylyakov, B. Lee, C. Jahnes, Y. Kwark, C. Baks, D. Kuchta, and J. Kash, “A 24-channel, 300 Gb/s, 8.2 pJ/bit, full-duplex fiber-coupled optical transceiver module based on a single ”holey” CMOS IC,” *J. Lightw. Technol.*, vol. 29, no. 4, pp. 542–553, 2011.
- [38] J. F. Seurin, C. L. Ghosh, V. Khalfin, A. Miglo, G. Y. Xu, J. D. Wynn, P. Pradhan, and L. A. D’Asaro, “High-power high-efficiency 2D VCSEL arrays,” in *Proc. SPIE*, vol. 6908, Feb. 2008, pp. 690 808–1–14.
- [39] W. Chow, K. Choquette, M. Crawford, K. Lear, and G. Hadley, “Design, fabrication, and performance of infrared and visible vertical-cavity surface-emitting lasers,” *IEEE J. Quantum Electron.*, vol. 33, no. 10, pp. 1810–1823, 1997.
- [40] S. Arafin, A. Bachmann, K. Kashani-Shirazi, and M. C. Amann, “Electrically pumped continuous-wave vertical-cavity surface-emitting lasers at  $\sim 2.6 \mu\text{m}$ ,” *Appl. Phys. Lett.*, vol. 95, no. 13, pp. 131 120–1–3, Sep. 2009.
- [41] S. Kalusniak, S. Sadofev, S. Halm, and F. Henneberger, “Vertical cavity surface emitting laser action of an all monolithic ZnO-based microcavity,” *Appl. Phys. Lett.*, vol. 98, no. 1, pp. 011 101–1–3, Jan. 2011.

- [42] Y. Higuchi, K. Omae, H. Matsumura, and T. Mukai, “Room-temperature CW lasing of a GaN-based vertical-cavity surface-emitting laser by current injection,” *Appl. Phys. Exp.*, vol. 1, no. 12, pp. 1 211 021–1 211 023, 2008.
- [43] K. Tai, L. Yang, Y. Wang, J. Wynn, and A. Cho, “Drastic reduction of series resistance in doped semiconductor distributed Bragg reflectors for surface-emitting lasers,” *Appl. Phys. Lett.*, vol. 56, no. 25, pp. 2496–2498, 1990.
- [44] M. G. Peters, B. J. Thibeault, D. B. Young, J. W. Scott, F. H. Peters, A. C. Gossard, and L. A. Coldren, “Band-gap engineered digital alloy interfaces for lower resistance vertical-cavity surface-emitting lasers,” *Appl. Phys. Lett.*, vol. 63, no. 25, pp. 3411–3413, 1993.
- [45] K. L. Lear and R. P. Schneider, Jr., “Uniparabolic mirror grading for vertical cavity surface emitting lasers,” *Appl. Phys. Lett.*, vol. 68, no. 5, pp. 605–607, Jan. 1996.
- [46] A. Haglund, J. Gustavsson, J. Vukusic, P. Modh, and A. Larsson, “Single fundamental-mode output power exceeding 6 mW from VCSELs with a shallow surface relief,” *IEEE Photon. Technol. Lett.*, vol. 16, no. 2, pp. 368–70, Feb. 2004.
- [47] K. Takaki, N. Iwai, K. Hiraiwa, S. Imai, H. Shimizu, T. Kageyama, Y. Kawakita, N. Tsukiji, and A. Kasukawa, “A recorded 62% PCE and low series and thermal resistance VCSEL with a double intra-cavity structure,” in *IEEE 21st International Semiconductor Laser Conference*, 2008.
- [48] C. Mateus, M. Huang, Y. Deng, A. Neureuther, and C. Chang-Hasnain, “Ultrabroadband mirror using low-index cladded subwavelength grating,” *IEEE Photon. Technol. Lett.*, vol. 16, no. 2, pp. 518–520, 2004.
- [49] M. Huang, Y. Zhou, and C. Chang-Hasnain, “A surface-emitting laser incorporating a high-index-contrast subwavelength grating,” *Nature Photon.*, vol. 1, no. 2, pp. 119–122, 2007.
- [50] J. W. Scott, R. S. Geels, S. W. Corzine, and L. A. Coldren, “Modeling temperature effects and spatial hole burning to optimize vertical-cavity surface-emitting laser performance,” *IEEE J. Quantum Electron.*, vol. 29, no. 5, pp. 1295–1308, 1993.
- [51] W. Nakwaski, “Thermal aspects of efficient operation of vertical-cavity surface-emitting lasers,” *Opt. Quantum Electron.*, vol. 28, no. 4, pp. 335–352, 1996.
- [52] P. Sundgren, R. von Wurtemberg, J. Berggren, M. Hammar, M. Ghisoni, V. Oscarsson, E. Odling, and J. Malmquist, “High-performance 1.3  $\mu\text{m}$

- InGaAs vertical cavity surface emitting lasers,” *Electron. Lett.*, vol. 39, no. 15, pp. 1128–9, Jul. 2003.
- [53] A. Mutig, G. Fiol, K. Potschke, P. Moser, D. Arsenijevic, V. Shchukin, N. Ledentsov, S. Mikhrin, I. Krestnikov, D. Livshits, A. Kovsh, F. Hopfer, and D. Bimberg, “Temperature-dependent small-signal analysis of high-speed high-temperature stable 980-nm VCSELs,” *IEEE J. Sel. Topics Quantum Electron.*, vol. 15, no. 3, pp. 679–686, 2009.
- [54] J. Jewell, A. Scherer, S. McCall, Y. Lee, S. Walker, J. Harbison, and L. Florez, “Low-threshold electrically pumped vertical-cavity surface-emitting microlasers,” *Electron. Lett.*, vol. 25, no. 17, pp. 1123–1124, 1989.
- [55] J. K. Guenter, R. A. Hawthorne III, D. N. Granville, M. K. Hibbs-Brenner, and R. A. Morgan, “Reliability of proton-implanted VCSELs for data communications,” in *Proc. SPIE*, M. Fallahi and S. C. Wang, Eds., vol. 2683, no. 1, 1996, pp. 102–113.
- [56] N. Dutta, L. Tu, G. Hasnain, G. Zydzik, Y. Wang, and A. Cho, “Anomalous temporal response of gain guided surface emitting lasers,” *Electron. Lett.*, vol. 27, no. 3, pp. 208–210, 1991.
- [57] B. Hawkins, R. Hawthorne III, J. Guenter, J. Tatum, and J. Biard, “Reliability of various size oxide aperture VCSELs,” in *Proc. 52nd Electronic Components and Technology Conference*, 2002, pp. 540–550.
- [58] W. Hofmann, M. Müller, A. Nadochiy, C. Meltzer, A. Mutig, G. Böhm, J. Rosskopf, D. Bimberg, M.-C. Amann, and C. Chang-Hasnain, “22-Gb/s long wavelength VCSELs,” *Opt. Exp.*, vol. 17, no. 20, pp. 17 547–17 554, Sep. 2009.
- [59] W. Hofmann, M. Müller, P. Wolf, A. Mutig, T. Grundl, G. Böhm, D. Bimberg, and M.-C. Amann, “40 Gbit/s modulation of 1550 nm VCSEL,” *Electron. Lett.*, vol. 47, no. 4, pp. 270–271, 2011.
- [60] M. Ortsiefer, R. Shau, G. Böhm, F. Köhler, and M.-C. Aman, “Low-threshold index-guided 1.5  $\mu\text{m}$  long-wavelength vertical-cavity surface-emitting laser with high efficiency,” *Appl. Phys. Lett.*, vol. 76, no. 16, pp. 2179–2181, 2000.
- [61] N. Suzuki, T. Anan, H. Hatakeyama, and M. Tsuji, “Low resistance tunnel junctions with type-II heterostructures,” *Appl. Phys. Lett.*, vol. 88, no. 23, pp. 231 103–1–3, 2006.
- [62] K. Yashiki, N. Suzuki, K. Fukatsu, T. Anan, H. Hatakeyama, and M. Tsuji, “1.1- $\mu\text{m}$ -range low-resistance InGaAs quantum-well vertical-cavity surface-emitting lasers with a buried type-II tunnel junction,” *Jpn. J. Appl. Phys.*, vol. 46, no. 20-24, pp. L512–L514, 2007.

- [63] Y. Satuby and M. Orenstein, "Mode-coupling effects on the small-signal modulation of multitransverse-mode vertical-cavity semiconductor lasers," *IEEE J. Quantum Electron.*, vol. 35, no. 6, pp. 944–954, 1999.
- [64] L.-G. Zei, S. Ebers, J.-R. Kropp, and K. Petermann, "Noise performance of multimode VCSELs," *J. Lightw. Technol.*, vol. 19, no. 6, pp. 884–892, 2001.
- [65] R. Nagarajan, M. Ishikawa, T. Fukushima, R. S. Geels, and J. E. Bowers, "High speed quantum-well lasers and carrier transport effects," *IEEE J. Quantum Electron.*, vol. 28, no. 10, pp. 1990–2008, 1992.
- [66] L. Coldren and S. Corzine, *Diode Lasers and Photonic Integrated Circuits*. John Wiley & Sons, Inc., 1995.
- [67] A. Tomita and A. Suzuki, "A new density matrix theory for semiconductor lasers, including non-Markovian intraband relaxation and its application to nonlinear gain," *IEEE J. Quantum Electron.*, vol. 27, no. 6, pp. 1630–1641, 1991.
- [68] M. Willatzen, T. Takahashi, and Y. Arakawa, "Nonlinear gain effects due to carrier heating and spectral holeburning in strained-quantum-well lasers," *IEEE Photon. Technol. Lett.*, vol. 4, no. 7, pp. 682–685, 1992.
- [69] R. Nagarajan and J. E. Bowers, *Semiconductor Lasers I: Fundamentals*, E. Kapon, Ed. Academic Press, 1999.
- [70] R. Olshansky, P. Hill, V. Lanzisera, and W. Powazinik, "Frequency response of 1.3  $\mu\text{m}$  InGaAsP high speed semiconductor lasers," *IEEE J. Quantum Electron.*, vol. 23, no. 9, pp. 1410–1418, 1987.
- [71] D. Tauber, G. Wang, R. Geels, J. Bowers, and L. Coldren, "Large and small signal dynamics of vertical cavity surface emitting lasers," *Appl. Phys. Lett.*, vol. 62, no. 4, pp. 325–327, 1993.
- [72] E. O'Reilly and A. Adams, "Band-structure engineering in strained semiconductor lasers," *IEEE J. Quantum Electron.*, vol. 30, no. 2, pp. 366–379, 1994.
- [73] S. Offsey, W. Schaff, P. Tasker, and L. Eastman, "Optical and microwave performance of GaAs-AlGaAs and strained layer InGaAs-GaAs-AlGaAs graded index separate confinement heterostructure single quantum well lasers," *IEEE Photon. Technol. Lett.*, vol. 2, no. 1, pp. 9–11, 1990.
- [74] J. D. Ralston, S. Weisser, I. Esquivias, E. C. Larkins, J. Rosenzweig, P. J. Tasker, and J. Fleissner, "Control of differential gain, nonlinear gain, and damping factor for high-speed application of GaAs-Based MQW lasers," *IEEE J. Quantum Electron.*, vol. 29, no. 6, pp. 1648–1658, 1993.

- [75] K. Kamite, H. Sudo, M. Yano, H. Ishikawa, and H. Imai, “Ultra-high speed InGaAsP/InP DFB lasers emitting at  $1.3\ \mu\text{m}$  wavelength,” *IEEE J. Quantum Electron.*, vol. 23, no. 6, pp. 1054–1058, 1987.
- [76] L. Lester, S. O’Keefe, W. Schaff, and L. Eastman, “Multiquantum well strained-layer lasers with improved low frequency response and very low damping,” *Electron. Lett.*, vol. 28, no. 4, pp. 383–385, 1992.
- [77] Y. Liu, W.-C. Ng, F. Oyafuso, B. Klein, and K. Hess, “Simulating the modulation response of VCSELs: The effects of diffusion capacitance and spatial hole-burning,” *IEE Proc. Optoelectron.*, vol. 149, no. 4, pp. 182–188, 2002.
- [78] Y. Liu, W.-C. Ng, B. Klein, and K. Hess, “Effects of the spatial nonuniformity of optical transverse modes on the modulation response of vertical-cavity surface-emitting lasers,” *IEEE J. Quantum Electron.*, vol. 39, no. 1, pp. 99–108, 2003.
- [79] Y. Chang, H. Kuo, F.-I. Lai, K. Tzeng, H. Yu, C. Sung, H. Yang, and S. Wang, “High speed ( $>13\ \text{GHz}$ ) modulation of 850 nm vertical cavity surface emitting lasers (VCSELs) with tapered oxide confined layer,” *IEE Proc. Optoelectron.*, vol. 152, no. 3, pp. 170–3, Jun. 2005.
- [80] J. Shah, “Hot carriers in quasi-2-D polar semiconductors,” *IEEE J. Quantum Electron.*, vol. 22, no. 9, pp. 1728–1743, 1986.
- [81] R. Safaisini, J. Joseph, D. Louderback, X. Jin, A. Al-Omari, and K. Lear, “Temperature Dependence of 980-nm Oxide-Confined VCSEL Dynamics,” *IEEE Photon. Technol. Lett.*, vol. 20, no. 14, pp. 1273–1275, 2008.
- [82] C. Wolfe, N. Holonyak, and G. Stillman, *Physical Properties of Semiconductors*. Prentice Hall, 1981.
- [83] E. Hegblom, D. Babic, B. Thibeault, and L. Coldren, “Scattering losses from dielectric apertures in vertical-cavity lasers,” *IEEE J. Sel. Topics Quantum Electron.*, vol. 3, no. 2, pp. 379–389, 1997.
- [84] E. R. Hegblom, N. M. Margalit, B. Thibeault, L. A. Coldren, and J. E. Bowers, “Current spreading in apertured vertical-cavity lasers,” in *Proc. SPIE*, vol. 3003, no. 1, Apr. 1997, pp. 176–180.
- [85] R. Naone, P. Floyd, D. Young, E. Hegblom, T. Strand, and L. Coldren, “Interdiffused quantum wells for lateral carrier confinement in VCSELs,” *IEEE J. Sel. Topics Quantum Electron.*, vol. 4, no. 4, pp. 706–714, 1998.
- [86] S. Adachi, “Lattice thermal resistivity of III-V compound alloys,” *J. Appl. Phys.*, vol. 54, no. 4, pp. 1844–1848, 1983.

- [87] Y.-A. Chang, F.-I. Lai, H.-C. Yu, H.-C. Kuo, L.-W. Lai, C.-L. Yu, and S.-C. Wang, "High temperature stability 850-nm  $\text{In}_{0.15}\text{Al}_{0.08}\text{Ga}_{0.77}\text{As}/\text{Al}_{0.3}\text{Ga}_{0.7}\text{As}$  vertical-cavity surface-emitting laser with single  $\text{Al}_{0.75}\text{Ga}_{0.25}\text{As}$  current blocking layer," *Jpn. J. Appl. Phys.*, vol. 44, no. 28-32, pp. L901–L902, 2005.
- [88] A. Al-Omari, G. Carey, S. Hallstein, J. Watson, G. Dang, and K. Lear, "Low thermal resistance high-speed top-emitting 980-nm VCSELs," *IEEE Photon. Technol. Lett.*, vol. 18, no. 11, pp. 1225–7, Jun. 2006.
- [89] R. Tucker and D. Pope, "Microwave circuit models of semiconductor injection lasers," *IEEE Trans. Microw. Theory and Tech.*, vol. 31, no. 3, pp. 289–294, 1983.
- [90] K. Lau and A. Yariv, "Ultra-high speed semiconductor lasers," *IEEE J. Quantum Electron.*, vol. 21, no. 2, pp. 121–138, 1985.
- [91] N. Nishiyama, M. Arai, S. Shinada, K. Suzuki, F. Koyama, and K. Iga, "Multi-oxide layer structure for single-mode operation in vertical-cavity surface-emitting lasers," *IEEE Photon. Technol. Lett.*, vol. 12, no. 6, pp. 606–608, 2000.
- [92] M. Azuchi, N. Jikutani, M. Arai, T. Kondo, and F. Koyama, "Multioxide layer vertical-cavity surface-emitting lasers with improved modulation bandwidth," in *Proc. Conference on Lasers and Electro-Optics*, vol. 1, 2003, p. 163, paper W2B-(2)-6.
- [93] Y. Chang, C. Wang, L. Johansson, and L. Coldren, "High-efficiency, high-speed VCSELs with deep oxidation layers," *Electron. Lett.*, vol. 42, no. 22, pp. 1281–1282, 2006.
- [94] H. Sewell, A. Chen, J. Finders, and M. Dusa, "Progress in extending immersion lithography for the 32 nm node and beyond," *Jpn. J. Appl. Phys.*, vol. 48, pp. 06FA01–1–6, 2009.
- [95] V. Sidorkin, A. van Run, A. van Langen-Suurling, A. Grigorescu, and E. van der Drift, "Towards 2-10 nm electron-beam lithography: a quantitative approach," *Microelectron. Eng.*, vol. 85, no. 5-6, pp. 805–809, 2008.
- [96] K. D. Choquette, K. Lear, R. Schneider Jr., K. Geib, J. Figiel, and R. Hull, "Fabrication and performance of selectively oxidized vertical-cavity lasers," *IEEE Photon. Technol. Lett.*, vol. 7, no. 11, pp. 1237–1239, 1995.
- [97] J.-H. Kim, D. Lim, K. Kim, G. Yang, K. Lim, and H. Lee, "Lateral wet oxidation of  $\text{Al}_x\text{Ga}_{1-x}\text{As}$ -GaAs depending on its structures," *Appl. Phys. Lett.*, vol. 69, no. 22, pp. 3357–3359, 1996.

- [98] O. Kjebon, R. Schatz, S. Lourdudoss, S. Nilsson, and B. Stalnacke, “Modulation response measurements and evaluation of MQW InGaAsP lasers of various designs,” in *Proc. SPIE*, vol. 2684, no. 1, Apr. 1996, pp. 138–152.
- [99] R. S. Tucker, J. M. Wiesenfeld, P. M. Downey, and J. E. Bowers, “Propagation delays and transition times in pulse-modulated semiconductor lasers,” *Appl. Phys. Lett.*, vol. 48, no. 25, pp. 1707–1709, Jun. 1986.
- [100] J. Redd, “Statistical confidence levels for error-probability estimates,” *Lightwave Magazine*, vol. 17, no. 5, April 2000.